ON PROPAGATION OF SHEAR CRIPPLING (KINKBAND) INSTABILITY IN A LONG IMPERFECT LAMINATED COMPOSITE CYLINDRICAL SHELL UNDER EXTERNAL PRESSURE

REAZ A. CHAUDHURI and DEOKJOO KIM†‡

Department of Materials Science and Engineering; †Department of Mechanical Engineering,
University of Utah, Salt Lake City, Utah 84112, U.S.A.

Abstract—A fully nonlinear analysis for prediction of shear crippling (kinkband) type propagating instability in long thick laminated composite cylindrical shells is presented. The primary accomplishment of the present investigation is prediction of equilibrium paths, which are often unstable, in the presence of interlaminar shear deformation, and which usually deviate from the classical lamination theory (CLT)-based equilibrium paths, representing global or structural level stability. A nonlinear finite element methodology, based on a three-dimensional hypothesis, known as layerwise linear displacement distribution theory (LLDT) and the total Lagrangian formulation, is developed to predict the aforementioned instability behavior of long laminated thick cylindrical shell type structures and evaluate failure modes when radial/hydrostatic compressive loads are applied. The most important computational feature is the successful implementation of an incremental displacement control scheme beyond the limit point to compute the unstable postbuckling path. A long (plane strain) thick laminated composite [90/0/90] imperfect cylinder is investigated with the objective of analytically studying its premature compressive failure behavior. Thickness effect (i.e. interlaminar shear/normal deformation) is clearly responsible for causing the appearance of limit point on the postbuckling equilibrium path, thus lowering the load carrying capability of the long composite cylinder, and localizing the failure pattern, which is associated with spontaneous breaking of the periodicity of classical or modal buckling patterns. In analogy to the phase transition phenomena, Maxwell construction is employed to (a) correct the unphysical negative slope of the computed equilibrium paths encountered in the case of thicker cylinders modeled by the finite elements methods that fail to include micro-structural defects, such as fiber waviness or misalignments, and (b) to compute the propagating pressure responsible for interlaminar shear crippling or kinkband type propagating instability. This type of instability triggered by the combined effect of interlaminar shear/normal deformation and geometric imperfections, such as fiber misalignment, appears to be one of the dominant compressive failure modes for moderately thick and thick cylinders with radius-to-thickness ratio below the corresponding critical value. A three-dimensional theory, such as the LLDT, is essential for capturing the interlaminar shear crippling type propagating instability. © 1997 Elsevier Science Ltd

NOMENCLATURE

$[A]$	Diagonal matrix composed of Aitken acceleration factors
$[\bar{B}_{LL}]$	Linear differential operator matrix relating the linear incremental strain components to incremental displacement components
$[B_{NL}]$	Linear differential operator matrix relating the linearized incremental strain components to incremental displacement components
$[B_{NN}]$	Linear differential operator matrix relating the nonlinear incremental strain components to incremental displacement components
$\mathbf{b}$	Binormal vector
b, t	Subscript or superscript indicating the bottom and top surface, respectively
C_{ijrs}	Elastic stiffness (material property) tensor
ds, ds_0	Length of time segment on a deformed and undeformed surface, respectively
$^0 dV$	Infinitesimal control volume with respect to the initial configuration
E_m, v_m	Young's modulus and Poisson's ratio, respectively, of the matrix material
E_{LT}, E_{TT}, v_{LT}	Longitudinal and transverse Young's moduli, and major Poisson's ratio, respectively, of a lamina
$\mathbf{e}_1$, $\mathbf{e}_2$	Unit tangent vectors along the coordinate directions
$_0\bar{e}_{ij}^L$	Linear incremental component of the 6×1 strain vector
$_0\bar{e}_{ij}^N$	Linearized incremental component of the 6×1 strain vector
$\{f_L\}$	Applied load vector
$^{t+\Delta t}\{f_L\}$	Applied load vector at the time $t + \Delta t$
$\{f_N\}$	Nonlinear internal force vector

‡ Current address : Agency for Defense Development, Taejon, Korea.

$^{t+\Delta t}\{f_N\}^{(i)}$ — Nonlinear internal force vector at the i-th iteration of the time step between t and $t+\Delta t$

G_{LT}, G_{TT} — Longitudinal and transverse shear moduli, respectively

$\mathbf{g}_k$ — Orthogonal base vector in the k-th direction

g_{ij}, g^{ij} — Components of metric and associated metric tensors, respectively

$g_k^{(i)}$ — Coefficient of the first fundamental differential quadratic form of the bottom surface of the i-th layer in the k-th direction, $k = 1, 2$

h_i, h — Thickness of the i-th lamina and the laminated shell, respectively

$[K_L]$ — Linear global stiffness matrix

$[K_N]$ — Nonlinear contribution to the global geometric stiffness matrix

L — Length of a composite cylinder test specimen; also, subscript indicating the longitudinal direction of a lamina

m_k — Half bandwidth of the total stiffness matrix

N — Total number of elements

NL, NS — Number of elements for each layer and number of layers, respectively

NT — Number of elements in the circumferential direction

$\mathbf{n}$ — Unit normal vector for the surface with respect to the fixed coordinate system

$\{^{t+\Delta t}\mathbf{n}^{(NS+1)}\}$ — Normal direction vector of the loaded surface (NS) evaluated at the first iteration of each load step when hydrostatic load is applied

P — Uniform hydrostatic pressure

p_{cr} — Classical buckling pressure of a long cylinder

p_P — Propagating pressure for shear crippling for kinkband instability in a long cylinder

$[Q], [\bar{Q}]$ — Elastic stiffness (material property) matrix for an orthotropic and anisotropic layer, respectively

$Q_{ij}^{(k)}, \bar{Q}_{ij}^{(k)}$ — Stiffness matrix components of the k-th orthotropic and anisotropic layer, respectively

$\{_0Q\}^{(i)}$ — Incremental displacement vector due to the applied load vector

$\mathbf{R}$ — Position vector of an arbitrary point at distance from the bottom surface of the i-th layer

R_i — Inner radius of a long perfect cylinder (plane strain ring)

$^{t+\Delta t}\mathscr{R}$ — External virtual work done on a body

$\{_0R\}^{(i)}$ — Incremental displacement vector due to the residual force vector

$\mathbf{r}$ — Position vector of an arbitrary point on the bottom surface of the i-th layer

$r_0(\theta), r(\theta)$ — Radial coordinates of the innermost (bottom) surface of an undeformed and deformed imperfect cylinder, respectively

$^{t+\Delta t}S$ — Loading surface area evaluated at the first iteration of each load step when hydrostatic pressure is applied

$_0S_{ij}^{(k)}$ — Incremental stress component of the k-th layer

$_0^{t+\Delta t}S_{ij}$ — Second Piola–Kirchhoff stress tensor at time $t+\Delta t$ evaluated with respect to the initial configuration

$_0^t\hat{S}_{ij}$ — 9×9 stress matrix evaluated at time t

$_0^t\bar{S}_{ij}$ — 6×1 stress vector evaluated at time t

$[_0^{t+\Delta t}\bar{S}^{(k)}]^{(i-1)}$ — Element stress vector of the k-th layer evaluated at the $(i-1)$th iteration of each load step

T — Superscript indicating the transpose of the matrix; also subscript indicating the transverse direction of a lamina

t — Time as an index

$\mathbf{t}$ — Tangent vector

u_k, u^k — Covariant and contravariant components of the displacement vector, respectively

$_0u_b^{(i)}, _0v_b^{(i)}, _0w_b^{(i)}$ — Incremental displacement components at a point on the bottom surface of the i-th layer in x^1 (or x), x^2 (or θ), and z directions, respectively

$_0u_t^{(i)}, _0v_t^{(i)}, _0w_t^{(i)}$ — Incremental displacement components at a point on the top surface of the i-th layer in x^1 (or x), x^2 (or θ), and z directions, respectively

$_0U_{bk}^{(i)}, _0V_{bk}^{(i)}, _0W_{bk}^{(i)}$ — Incremental nodal displacement components at the k-th node on the bottom surface of the i-th layer in x^1 (or x), x^2 (or θ), and z directions, respectively

$_0U_{tk}^{(i)}, _0V_{tk}^{(i)}, _0W_{tk}^{(i)}$ — Incremental nodal displacement components at the k-th node on the top surface of the i-th layer in x^1 (or x), x^2 (or θ), and z directions, respectively

$^{t+\Delta t}\{V\}^{(i)}$ — Total displacement vector at the i-th iteration of the time step between t and $t+\Delta t$

$_0V_q$ — The q-th displacement prescribed at each time step for the displacement increment method

v_i — The i-th physical component of the displacement vector, $i = 1,2,3$

w_0 — Amplitude of modal imperfection of a long cylinder

$x^{(i)}, \theta^{(i)}, z^{(i)}$ — Coordinates of a point in the element of the i-th layer in terms of r and s

α, β — Lines of curvature of the shell reference (bottom) surface

ε_{ij} — Physical component of the Green–Lagrange strain tensor

$_0\varepsilon_{ij}^{(k)}$ — Incremental strain component of the k-th layer

$_0^{t+\Delta t}\varepsilon_{ij}$ — Total Green–Lagrangian strain tensor evaluated with respect to the initial configuration at time $t+\Delta t$

$\varepsilon_f, \varepsilon_c$ — Force and energy convergence criteria, respectively

$\boldsymbol{\kappa}$ — Principal curvature vector

$_0\lambda^{(i)}$ — Incremental load scale factor due to the prescribed displacement component

Γ_{lm}^k — Christoffel symbol of the second kind

$\hat{\eta}_{ki}, \delta\hat{\eta}_{ki}$ — 9×1 nonlinear strain component vector and its variation, respectively

γ_{ij} — Covariant component of the Green–Lagrangian strain tensor

$[\Phi]$ — Quadratic global interpolation function matrix

$\psi_k(r, s)$ — Quadratic element interpolation function in terms of r and s

$\rho_k^{(i)}$ — The k-th principal radius of curvature of the i-th shell layer

$\rho, \rho^{(i)}$ — Radius of curvature of the inner surface of an imperfect cylinder and its i-th layer, respectively

θ — Angle measured from the global x axis

τ — Torsion.

1. INTRODUCTION

In recent years, advanced composite materials have increasingly been used for structural (e.g. thin/thick shells) applications where high strength-to-weight and stiffness-to-weight ratios, corrosion resistance, long fatigue life, etc. are required. Currently, the primary usage of advanced composite materials is for aerospace applications. These usually require thin-section structures subjected to primarily tensile loading conditions, the one notable exception being the aircraft wing structure, which is subjected to bending. In contrast, the composites used in hydrospace applications must, by necessity, be thick-sections in order to avoid catastrophic collapse caused by global (structural) buckling, and must sustain large hydrostatic compressive loads. Their deformation and failure behavior (e.g. buckling/postbuckling, shear kinking, etc.) are of great concern to structural designers.

The compressive response of thin shell structures is known to be primarily characterized by the stability of equilibrium at the macro-structural level. The loss of stability of an isotropic thin shell-type structure under external pressure has been studied extensively during the last five decades, and is relatively well understood (see Simitses, 1986). The first investigator to systematically develop a stability theory pertaining to the initial postbuckling behavior of a continuous linear elastic system was Koiter (1945). Koiter was primarily concerned with the stability (or lack thereof) of equilibrium states in the neighborhood of the buckling load (bifurcation point). Another important ingredient of Koiter's theory is the investigation of the effect of a small imperfection whose shape is the same as that of a classical buckling mode. Tvergaard and Needleman (1980) have studied the possibility of localization of uniform buckling pattern for a class of isotropic thin structures with modal imperfections in which the initial buckling mode is periodic. Their analyses, carried out for an imperfect column on a softening foundation and an elastic-plastic imperfect thin plate strip under axial compression, demonstrate that the basic mechanism of localization involves a bifurcation, subsequent to the maximum (limit) load point. The finite element analysis of the elastic-plastic imperfect thin strip under axial compression shows the development of localization for the case of a low hardening material, whereas localization does not occur in the otherwise same plate of a high hardening material for which no limit load is reached. Chater and Hutchinson (1984) have evaluated the quasi-static, steady-state (critical) propagation pressure for two examples—(i) bulge propagation down the length of a cylindrical rubber balloon subjected to internal pressure, and (ii) buckle propagation in a long pipe under external pressure. Propagating instabilities are initiated from local imperfections that locally weaken the structure, and cause local change in geometry (collapse). Very much like a set of dominoes (Bert, 1986), once the geometric integrity of a structure is compromised, the instability has the potential of spreading over the whole structure (Kyriakides, 1994).

Feasibility studies relating to use of fiber-reinforced composite materials in deep submergence pressure hull applications have been carried out at the NSWC, Carderock, since the 1960s. Recently, Garala (1986; 1989), and Garala and Chaudhuri (1993) have carried out extensive experimental and theoretical evaluations of advanced (e.g. carbon/epoxy) composite thick unstiffened cylindrical specimens (e.g. inner radius to thickness ratio, $R_i/h = 6.0$ and length, $L = 8.0''$) subjected to external pressure loading. They have reported details of (a) fabrication methods of cylinders, (b) experimental data on collapse pressures, strains and damage assessment, obtained using strain gages and acoustic emission (AE), and (c) structural analyses for prediction of stresses and collapse pressures, performed using standard finite element codes. The key observations can be summarized as follows: (a) the observed hoop stress level of approximately 84 ksi is considerably lower than the estimated value of 160 ksi based on thin-section composites experience (using the rule of mixtures with 240 ksi *in situ* fiber strength); (b) unacceptably low failure external pressure in the 12 ksi range has generally been observed with certain exceptions, as compared to the computed value of 22 ksi based on the above estimated hoop stress value; (c) a considerable amount of scatter has been observed in the test data; and (d) fabrication defects are believed to have a detrimental effect on the compressive strength. Abdallah *et al.* (1990) have conducted a series of innovative tests on thick composite rings under external pressure, using an especially designed bladder and obtained extensive data by means of strain gages,

AE, photoelasticity and Moire interferometry. In general, although the ring specimens failed at pressures 10–25% higher than their cylindrical counterparts made of the same material systems, almost identical failure mechanisms are observed in both sets of specimens.

Starnes and Williams (1982) have reported a shear crippling type of failure to be prevalent in the vicinity of a hole weakening a laminate prior to catastrophic failure. Waas *et al.* (1990) have carefully monitored in real time the compressive damage initiation and propagation in a laminated plate through holographic interferometry and photomicrography of the hole surface, and have concluded that failure is initiated as a localized microbuckling/kinking instability in the 0°-plies at the hole surface followed by delamination. Chaudhuri (1991) has identified the formation and propagation of fiber kinkbands at the microscopic level triggered by fiber misalignment defects formed during the manufacturing process, leading to the shear crippling failure at the macroscopic level to be the dominant (lowest energy) compressive failure mode for the thick-section $[90_2/0]_m$ type composite cylinders. Initial fiber misalignment, ultimate fiber strain and the two transverse shear moduli, G_{LT} and G_{TT}, of the laminate, were found to be the key parameters limiting the compressive strength of the aforementioned thick-section composite laminates. Regardless of the event or sequence of events that may act as precursor(s), kinkband formation, once triggered, will in general be the dominant (lowest energy) failure mode, especially in the presence of such defects as fiber waviness or misalignment, resin rich areas, etc. Numerical results for carbon/epoxy laminates demonstrate their extreme sensitivity to initial fiber misalignment defects, which are, at least partially, responsible for the lowering of the compressive strength of the thick cylinders tested by Garala (1989) and the observed scatter in his test data.

The aforementioned understanding of the microscopic behavior of carbon/epoxy composites notwithstanding some nagging questions persist. Of special interest is the sensitivity to interlaminar shear/normal deformation (thickness effect), especially in the presence of geometrical defects such as fiber misalignment or waviness, and out-of-roundedness. These defects are apt to be generated during a large scale fabrication process of thick-section laminated shells. The large discrepancy between the observed experimental data and the corresponding analytical predictions has so far remained an enigma, because of a lack of availability of an analytical tool for accurate prediction of the structural behavior in the advanced nonlinear regime, especially when the radius to thickness ratio decreases. Recent surveys, e.g. Simitses (1986), and Noor and Burton (1990), reveal that investigations relating to the response of a composite cylinder subjected to external pressure are still restricted to the classical approach that can yield only the uniform buckling/post-buckling patterns. Little attention has been paid to the interlaminar shear crippling (kinkband) type quasi-statically propagating instability modes that are experimentally observed. Therefore, the overall goal of the present investigation is to fill this analytical gap, and to identify basic mechanisms for interlaminar shear crippling (kinkband) type propagating instability modes causing "premature" failure of the advanced composite cylinders under investigation. The classical approach which is concerned with the uniform buckling/post-buckling pattern, although deemed sufficient for the design of most structures, is inadequate when it comes to propagating type instabilities, such as kinkbands propagating along the cylinder length, very much the same way as the propagating bulges and buckles investigated by Chater and Hutchinson (1984), and Kyriakides (1994) among others.

The present analysis includes all the nonlinear terms in the kinematic equations and utilizes the total Lagrangian formulation in the constitutive equations and incremental equilibrium equations. A nonlinear thick cylindrical shell finite element methodology is developed in order to obtain the discretized system equations. A cylindrically curved 16-node layer-element is used, which is based on an assumed quadratic displacement field (in surface-parallel coordinates) and the assumption of layerwise linear displacements distribution through thickness (LLDT). The Newton–Raphson iteration scheme in conjunction with Aitken acceleration is used to obtain the limit point or collapse pressure. The postbuckling behavior is obtained by an incremental displacement control scheme rather than the usual incremental force control scheme beyond the limit point in order to accurately predict an unstable postbuckling equilibrium path.

The primary objective of the present investigation is to study the thickness effect responsible for causing the appearance of limit point on the postbuckling equilibrium path, thus lowering the load carrying capability of the long composite cylinder, and localizing the failure pattern. The combined effects of modal imperfections and interlaminar shear/normal deformation on the localization and propagation of shear crippling (kinkband) type instability phenomenon, in long [90/0/90] cylinders (plane strain rings) are numerically investigated in detail. In analogy to the phase transition phenomena, Maxwell construction is employed to (a) correct the unphysical negative slope of the computed equilibrium paths encountered in the case of thicker cylinders modeled by the finite elements methods that fail to include micro-structural defects, such as fiber waviness or misalignments, and (b) to compute the propagating pressure responsible for interlaminar shear crippling or kinkband type propagating instability in moderately thick and thick cylinders with radius-to-thickness ratio below the corresponding critical value.

2. KINEMATIC RELATIONS OF A SHELL

General theory of elasticity with finite strain

Figure 1 shows the schematic of a laminated general shell. An arbitrary point Q_0 in the i-th layer undergoing a displacement **u** is considered. The Lagrangian coordinate system refers to a particle motion given by $\mathbf{X} = \mathbf{X}(\mathbf{x}, t)$, where **x** denotes an orthogonal curvilinear coordinate system, defining the position vector of the point Q_0, at time $t = t_0$ in the undeformed state, whereas **X** denotes the corresponding position vector of the point Q in the deformed state, at time t. The difference between the squares of line segments, $(\mathrm{d}s)^2$ and $(\mathrm{d}S)^2$ on the undeformed and deformed surfaces, respectively, is the measure of strain given by (Green and Zerna, 1968)

$$(\mathrm{d}S)^2 - (\mathrm{d}s)^2 = 2\gamma_{ij}\,\mathrm{d}x_i\,\mathrm{d}x_j \tag{1}$$

where γ_{ij} is given by

$$\gamma_{ij} = \tfrac{1}{2}([u_{i,j} - u_k\Gamma_{ij}^k] + [u_{j,i} - u_k\Gamma_{ij}^k] + [u_{k,i}u_{,j}^k - u_k\Gamma_{im}^k u_{,j}^m + u_{k,i}\Gamma_{lj}^k u^l - u_k u^l\Gamma_{im}^k\Gamma_{lj}^m]). \tag{2}$$

The physical component v_i of the displacement vector, **u**, for an orthogonal coordinate system can be written as

$$v_i = u_i\sqrt{g^{ii}} = u^i\sqrt{g_{ii}} \quad \text{(no sum on } i\text{)}. \tag{3}$$

A physical component ε_{ij} of the second-order tensor γ_{ij} can also be obtained as

$$\varepsilon_{ij} = \sqrt{g^{ii}g^{jj}\gamma_{ij}} \quad \text{(no sum on } i,j\text{)}. \tag{4}$$

Substitution of eqns (2) and (3) into eqn (4) yields

$$\varepsilon_{ij} = \frac{1}{2}\sqrt{g^{ii}g^{jj}}\left(\left[\left(\frac{v_i}{\sqrt{g^{ii}}}\right)_{,j} - \left(\frac{v_k}{\sqrt{g^{kk}}}\right)\Gamma_{ij}^k\right] + \left[\left(\frac{v_j}{\sqrt{g^{jj}}}\right)_{,i} - \left(\frac{v_k}{g^{kk}}\right)\Gamma_{ij}^k\right]\right.$$

$$+ \left[\left(\frac{v_k}{\sqrt{g^{kk}}}\right)_{,j}\left(\frac{v_k}{\sqrt{g^{kk}}}\right)_{,j} - \left(\frac{v_k}{\sqrt{g^{kk}}}\right)\Gamma_{im}^k\left(\frac{v_m}{\sqrt{g_{mm}}}\right)_{,j} + \left(\frac{v_k}{\sqrt{g^{kk}}}\right)_{,i}\Gamma_{lj}^k\left(\frac{v_l}{\sqrt{g_{ll}}}\right)\right.$$

$$\left.\left. - \left(\frac{v_k}{\sqrt{g^{kk}}}\right)\left(\frac{v_l}{\sqrt{g_{ll}}}\right)\Gamma_{im}^k\Gamma_{lj}^m\right]\right). \tag{5}$$
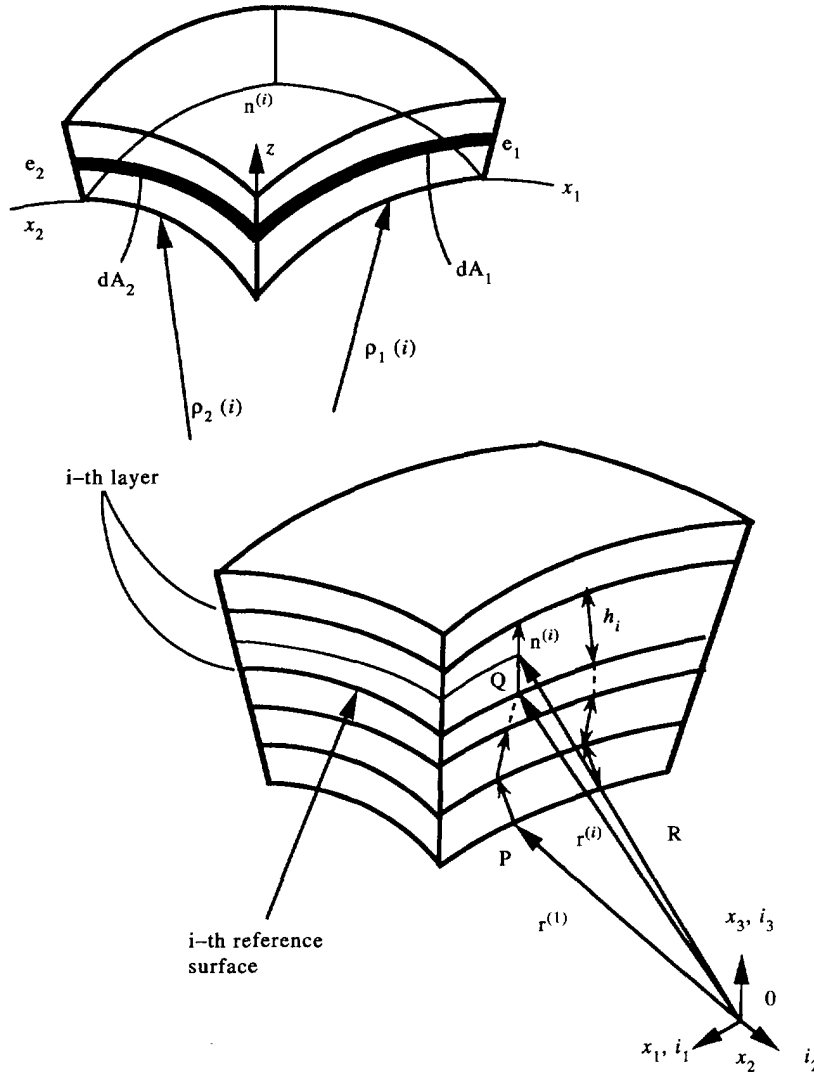
Fig. 1. Geometry of a laminated general shell (infinitesimal) element.

Surface geometry of a general shell

An undeformed bottom surface of the i-th layer described by $\mathbf{r}^{(i)} = \mathbf{r}^{(i)}(x^1, x^2, 0)$ where x^1, x^2 are orthogonal curvilinear coordinates attached to this surface is considered. For simplicity, the superscript i denoting the i-th layer would be omitted in this section. The distance $\mathrm{d}s$, between points $(x^1, x^2, 0)$ and $(x^1 + \mathrm{d}x^1, x^2 + \mathrm{d}x^2, 0)$ located on the bottom surface of the i-th layer is determined by

$$(\mathrm{d}s)^2 = \mathbf{dr} \cdot \mathbf{dr} = (g_1)^2 (\mathrm{d}x^1)^2 + 2g_1 g_2 \cos\chi \, \mathrm{d}x^1 \, \mathrm{d}x^2 + (g_2)^2 (\mathrm{d}x^2)^2 \tag{6}$$

in which $\mathbf{dr} = \mathbf{r}_{,1} \mathrm{d}x^1 + \mathbf{r}_{,2} \mathrm{d}x^2$ with $\mathbf{r}_{,j} = \partial \mathbf{r}/\partial x^j$ tangent to the x^i coordinate lines. The g_1 and g_2 are also called the coefficients of the first fundamental differential quadratic form of the surface, which are written as

$$(g_1)^2 = \mathbf{r}_{,1} \cdot \mathbf{r}_{,1} \, ; \quad (g_2)^2 = \mathbf{r}_{,2} \cdot \mathbf{r}_{,2} \, ; \quad \cos\chi = \frac{\mathbf{r}_{,1}}{g_1} \cdot \frac{\mathbf{r}_{,2}}{g_2} = 0. \tag{7}$$

The layer unit normal director $\mathbf{n}$ of the surface relative to the fixed coordinate system at time t, is given by
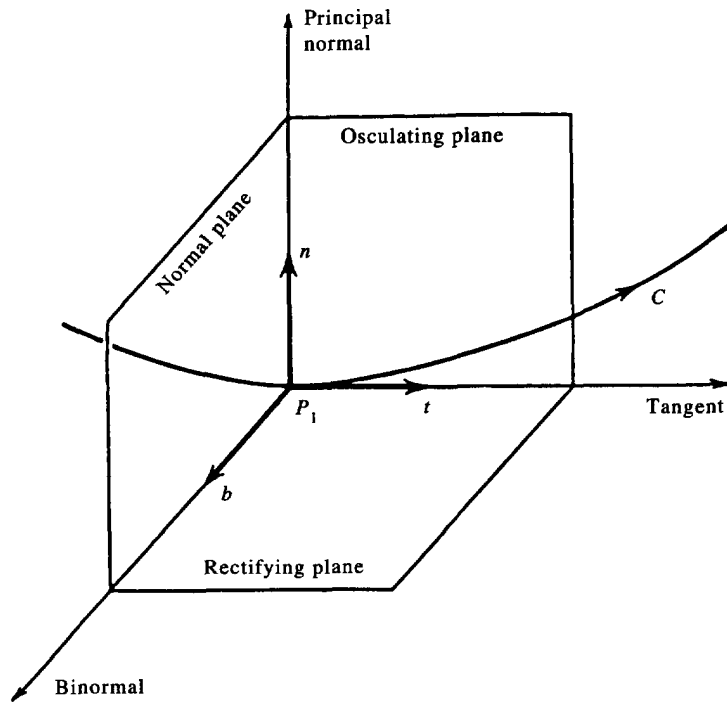
Fig. 2. Darboux's moving trihedron.

$$\mathbf{n} = \mathbf{e}_1 \times \mathbf{e}_2 = \frac{\mathbf{r}_{,1} \times \mathbf{r}_{,2}}{g_1 g_2} \tag{8a}$$

where the two unit tangent vectors $\mathbf{e}_1$ and $\mathbf{e}_2$ for a particular normal section C_i become

$$\mathbf{e}_1 = \frac{\mathbf{r}_{,1}}{g_1} \quad \text{and} \quad \mathbf{e}_2 = \frac{\mathbf{r}_{,2}}{g_2}, \tag{8b}$$

respectively, because $\mathbf{r}$ is a vector function of both x^1 and x^2.

The position vector, $\mathbf{R}$ of an arbitrary point Q at a distance z, from the bottom surface of the i-th layer, measured along the unit normal $\mathbf{n}$ is

$$\mathbf{R}(x^1, x^2, z) = \mathbf{r}(x^1, x^2, 0) + z\mathbf{n}(x^1, x^2) \tag{9}$$

where a layerwise coordinate z is conveniently introduced. The square of a line element $\mathrm{d}S$ between points (x^1, x^2, z) and $(x^1 + \mathrm{d}x^1, x^2 + \mathrm{d}x^2, z + \mathrm{d}z)$ is given by

$$(\mathrm{d}S)^2 = \mathrm{d}\mathbf{R} \cdot \mathrm{d}\mathbf{R} = (R_{,1}\, \mathrm{d}x^1 + R_{,2}\, \mathrm{d}x^2 + R_{,3}\, \mathrm{d}z) \cdot (R_{,1}\, \mathrm{d}x^1 + R_{,2}\, \mathrm{d}x^2 + R_{,3}\, \mathrm{d}z). \tag{10}$$

Partial differentiation of eqn (9) yields

$$\mathbf{R}_{,1} = \mathbf{r}_{,1} + z\mathbf{n}_{,1}; \quad \mathbf{R}_{,2} = \mathbf{r}_{,2} + z\mathbf{n}_{,2}; \quad \mathbf{R}_{,3} = \mathbf{n}. \tag{11}$$

Considering Darboux's moving trihedron (see Korn and Korn, 1968) as shown in Fig. 2, and referring to the Frenet formula

$$\frac{\mathrm{d}\mathbf{n}}{\mathrm{d}s} = -\tau\mathbf{b} + \kappa\mathbf{t} \tag{12}$$

it can be seen that the torsion τ vanishes because the binormal vector $\mathbf{b}$ does not change in

either magnitude or direction along an incremental length ds of the principal curvature κ where **t** is the tangent vector. Hence, eqn (12) becomes

$$\mathbf{dn} = \kappa \frac{\mathbf{dr}}{\mathrm{d}s} \mathrm{d}s. \tag{13}$$

The above equation may be written into components as

$$\mathbf{n}_{,1} = \kappa_1 \mathbf{r}_{,1} = \frac{g_1}{\rho_1}\mathbf{e}_1 \ ; \quad \mathbf{n}_{,2} = \kappa_2 \mathbf{r}_{,2} = \frac{g_2}{\rho_2}\mathbf{e}_2. \tag{14}$$

Substituting eqns (14) and (8b) into eqn (11) yields

$$\mathbf{R}_{,i} = \mathbf{r}_{,i} + z\mathbf{n}_{,i} = g_i\left(1 + \frac{z}{\rho_i}\right)\mathbf{e}_i \ ; \quad i = 1,2 \ (\text{no sum}) \ ; \quad \mathbf{R}_{,3} = \mathbf{n}. \tag{15}$$

Making use of these quantities, eqn (10) is simplified to

$$(\mathrm{d}S)^2 = (g_1)^2\left(1 + \frac{z}{\rho_1}\right)^2 (\mathrm{d}x^1)^2 + (g_2)^2\left(1 + \frac{z}{\rho_2}\right)^2 (\mathrm{d}x^2)^2 + (\mathrm{d}z)^2. \tag{16a}$$

On the other hand, the different form for $(\mathrm{d}S)^2$ of an arbitrary line element inside the shell can be easily formulated as in eqn (6), which is denoted by

$$(\mathrm{d}S)^2 = g_{11}(\mathrm{d}x^1)^2 + g_{22}(\mathrm{d}x^2)^2 + g_{33}(\mathrm{d}z)^2. \tag{16b}$$

Comparing the components of eqns (16a) and (16b), the following relations are obtained for the i-th layer of a laminated general shell:

$$g_\alpha^{(i)} = \sqrt{g_{11}} = g_1^{(i)}\left(1 + \frac{z}{\rho_1^{(i)}}\right); \quad g_\beta^{(i)} = \sqrt{g_{22}} = g_2^{(i)}\left(1 + \frac{z}{\rho_2^{(i)}}\right); \quad \sqrt{g_{33}} = 1. \tag{17}$$

Nonlinear kinematic relations for a cylindrical shell

A laminated general (not necessarily circular) cylindrical shell element is shown in Fig. 3. The following relations for a cylindrical shell are obtained from eqn (17):

$$\sqrt{g_{11}} = \sqrt{g_{33}} = 1 \ ; \quad g_\beta^{(i)} = \sqrt{g_{22}} = g_2^{(i)}\left(1 + \frac{z}{\rho^{(i)}}\right) = \rho^{(i)}\left(1 + \frac{z}{\rho^{(i)}}\right). \tag{18}$$

On substituting the physical components of the displacement vector **v** and the coefficients of the first fundamental differential quadratic form of the surface, given by eqn (18), into eqn (5), the components of the engineering nonlinear strain in terms of displacements at an arbitrary point inside the i-th layer are obtained as follows [the superscript (i) is dropped in the remainder of this section and the following one for notational convenience]:

$$\varepsilon_{11} = \frac{\partial u}{\partial x^1} + \frac{1}{2}\left[\left\{\frac{\partial u}{\partial x^1}\right\}^2 + \left\{\frac{\partial v}{\partial x^1}\right\}^2 + \left\{\frac{\partial w}{\partial x^1}\right\}^2\right] \tag{19a}$$

$$\varepsilon_{22} = \frac{1}{g_\beta}\left\{\frac{\partial v}{\partial x^2} + w\right\} + \frac{1}{2g_\beta^2}\left\{\frac{\partial v}{\partial x^2} + w\right\}^2 + \frac{1}{2g_\beta^2}\left\{\frac{\partial u}{\partial x^2}\right\}^2 + \frac{1}{2g_\beta^2}\left\{\frac{\partial w}{\partial x^2} - v\right\}^2 \tag{19b}$$
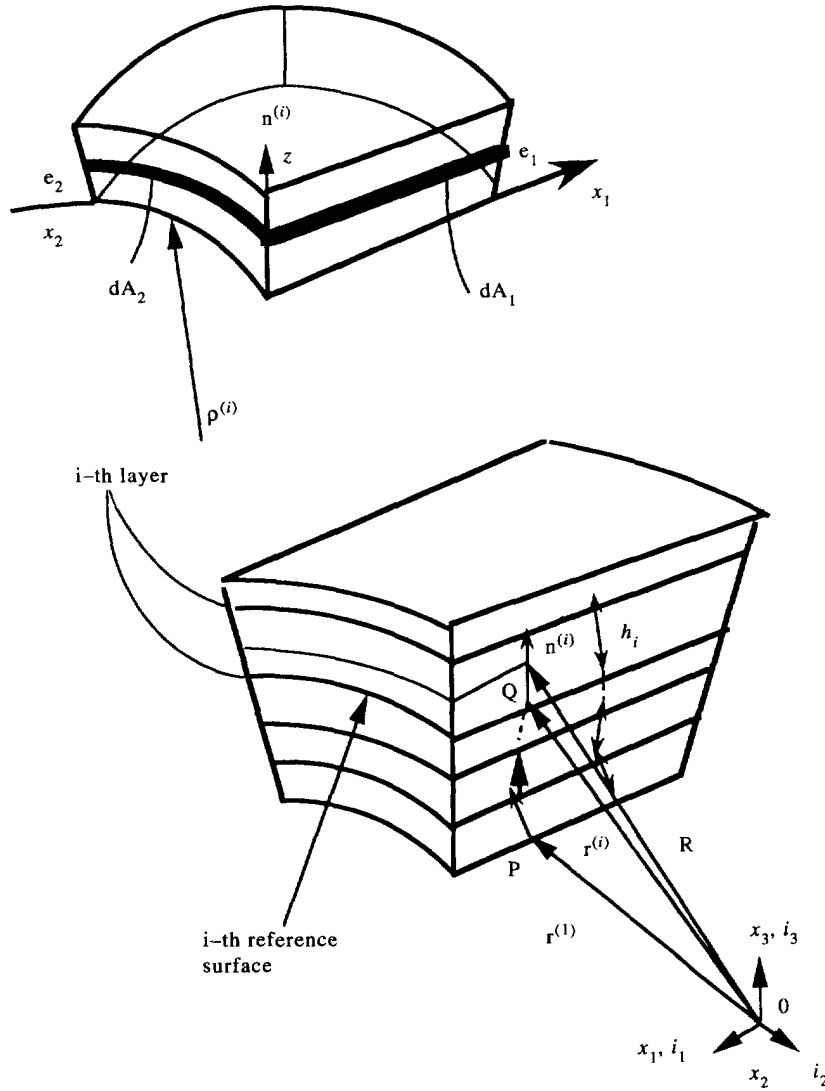
Fig. 3. Geometry of a laminated cylindrical shell (infinitesimal) element.

$$\varepsilon_{12} = \frac{\partial v}{\partial x^1} + \frac{1}{g_\beta}\frac{\partial u}{\partial x^2} + \frac{1}{g_\beta}\frac{\partial u}{\partial x^1}\frac{\partial u}{\partial x^2} + \frac{1}{g_\beta}\left\{\frac{\partial v}{\partial x^2}+w\right\}\frac{\partial v}{\partial x^1} + \frac{1}{g_\beta}\left\{\frac{\partial w}{\partial x^2}-v\right\}\frac{\partial w}{\partial x^1} \tag{19c}$$

$$\varepsilon_{33} = \frac{\partial w}{\partial z} + \frac{1}{2}\left(\frac{\partial u}{\partial z}\right)^2 + \frac{1}{2}\left(\frac{\partial v}{\partial z}\right)^2 + \frac{1}{2}\left(\frac{\partial w}{\partial z}\right)^2 \tag{19d}$$

$$\varepsilon_{13} = \frac{\partial w}{\partial x^1} + \frac{\partial u}{\partial z} + \frac{\partial u}{\partial x^1}\frac{\partial u}{\partial z} + \frac{\partial v}{\partial x^1}\frac{\partial v}{\partial z} + \frac{\partial w}{\partial x^1}\frac{\partial w}{\partial z} \tag{19e}$$

$$\varepsilon_{23} = \frac{1}{g_\beta}\left\{\frac{\partial w}{\partial x^2}-v\right\} + \frac{\partial v}{\partial z} + \frac{1}{g_\beta}\left\{\frac{\partial v}{\partial x^2}+w\right\}\frac{\partial v}{\partial z} + \frac{1}{g_\beta}\frac{\partial u}{\partial x^2}\frac{\partial u}{\partial z} + \frac{1}{g_\beta}\frac{\partial w}{\partial z}\left(\frac{\partial w}{\partial x^2}-v\right) \tag{19f}$$

where the physical components of the displacement vector v given by

$$v_1 = u(x^1,x^2,z); \quad v_2 = v(x^1,x^2,z); \quad v_3 = w(x^1,x^2,z) \tag{20}$$

have already been utilized.

3. LINEARIZED EQUATIONS OF MOTION—METHOD OF VIRTUAL WORK

The second Piola–Kirchhoff stress tensor is conjugate to the Green–Lagrange strain tensor in that their properties are invariant under rigid body motions. When the equilibrium of the body at time $t + \Delta t$ is first expressed using the principle of virtual displacements with tensor notation, the total Lagrangian formulation requires that

$$\int_{0_V} {}^{t+\Delta t}_0 S_{ij} \delta {}^{t+\Delta t}_0 \bar{\varepsilon}_{ij} \, {}^0 \mathrm{d}V = {}^{t+\Delta t} \mathscr{R} \tag{21}$$

where

$$ {}^{t+\Delta t}_0 S_{ij} = {}^t_0 S_{ij} + {}_0 S_{ij} \tag{22}$$

$$ {}^{t+\Delta t}_0 \bar{\varepsilon}_{ij} = {}^t_0 \bar{\varepsilon}_{ij} + {}_0 \bar{\varepsilon}_{ij} \, ; \quad {}_0 \bar{\varepsilon}_{ij} = {}_0 \bar{e}_{ij} + {}_0 \bar{\eta}_{ij}. \tag{23}$$

The quantities ${}_0 \bar{e}_{ij}, {}_0 \bar{\eta}_{ij}$ in eqn (23) also denote the linear and nonlinear incremental strains, respectively, that refer to the initial configuration. The linear strain vector $\{{}_0 \bar{e}_{ij}\}$ is here resolved into two parts that are the pure linear part, $\{{}_0 \bar{e}^L_{ij}\}$ and the linearized part, $\{{}_0 \bar{e}^N_{ij}\}$. Substituting eqns (22), (23) and the constitutive relations

$$ {}_0 S_{ij} = C_{ijrs} \, {}_0 \bar{\varepsilon}_{rs} \tag{24}$$

into the left hand side of eqn (21) finally yields the following:

$$\int_{0_V} ({}^t_0 S_{ij} + {}_0 S_{ij}) \delta ({}^t_0 \bar{\varepsilon}_{ij} + {}_0 \bar{\varepsilon}_{ij}) \, {}^0 \mathrm{d}V \cong \int_{0_V} C_{ijrs} \, {}_0 \bar{e}^L_{rs} \delta {}_0 \bar{e}^L_{ij} \, {}^0 \mathrm{d}V$$

$$+ \int_{0_V} C_{ijrs} \, {}_0 \bar{e}^N_{rs} \delta {}_0 \bar{e}^L_{ij} \, {}^0 \mathrm{d}V + \int_{0_V} C_{ijrs} \, {}_0 \bar{e}^L_{rs} \delta {}_0 \bar{e}^N_{ij} \, {}^0 \mathrm{d}V + \int_{0_V} C_{ijrs} \, {}_0 \bar{e}^N_{rs} \delta {}_0 \bar{e}^N_{ij} \, {}^0 \mathrm{d}V$$

$$+ \int_{0_V} \delta \bar{\eta}_{ki} \, {}^t_0 \hat{S}_{ij} \bar{\eta}_{kj} \, {}^0 \mathrm{d}V + \int_{0_V} {}^t_0 \bar{S}_{ij} \{ \delta_0 \bar{e}^L_{ij} + \delta_0 \bar{e}^N_{ij} \} \, {}^0 \mathrm{d}V \tag{25}$$

in which terms of degree two or higher in this equation are so small, compared with other terms that those terms can be neglected. Using eqns (19) and (23) each strain component in eqn (25) may be represented in the matrix form as follows:

$$\{ {}_0 \bar{e}^L \} = [B_{LL}] \{ {}_0 v \} \, ; \quad \{ {}_0 \bar{e}^N \} = [B_{NL}] \{ {}_0 v \} \, ; \quad \{ {}_0 \hat{\eta} \} = [B_{NN}] \{ {}_0 v \} \tag{26}$$

where

$$\{ {}_0 v \} = \{ {}_0 u \quad {}_0 v \quad {}_0 w \}^T \tag{27a}$$

$$\{ {}_0 \bar{e}^L \} = \{ {}_0 \bar{e}^L_{xx} \quad {}_0 \bar{e}^L_{\theta\theta} \quad {}_0 \bar{e}^L_{zz} \quad {}_0 \bar{e}^L_{z\theta} \quad {}_0 \bar{e}^L_{xz} \quad {}_0 \bar{e}^L_{x\theta} \}^T \tag{27b}$$

$$\{ {}_0 \bar{e}^N \} = \{ {}_0 \bar{e}^N_{xx} \quad {}_0 \bar{e}^N_{\theta\theta} \quad {}_0 \bar{e}^N_{zz} \quad {}_0 \bar{e}^N_{z\theta} \quad {}_0 \bar{e}^N_{xz} \quad {}_0 \bar{e}^N_{x\theta} \}^T \tag{27c}$$

$$\{ {}_0 \hat{\eta} \} = \{ {}_0 \bar{\eta}_{xx} \ {}_0 \bar{\eta}_{x\theta} \ {}_0 \bar{\eta}_{xz} \ {}_0 \bar{\eta}_{\theta x} \ {}_0 \bar{\eta}_{\theta\theta} \ {}_0 \bar{\eta}_{\theta z} \ {}_0 \bar{\eta}_{zx} \ {}_0 \bar{\eta}_{z\theta} \ {}_0 \bar{\eta}_{zz} \}^T. \tag{27d}$$

The differential operators, $[B_{LL}]$, $[B_{NL}]$ and $[B_{NN}]$, are as presented in eqns (A1), (A2), (A3a–c) and (A7), respectively, in the Appendix.

Because the variation in the strain components is equivalent to the use of virtual strains, the right hand side of eqn (21) is the virtual work done when the body is subjected to a virtual displacement at time $t + \Delta t$. The corresponding virtual work is denoted by
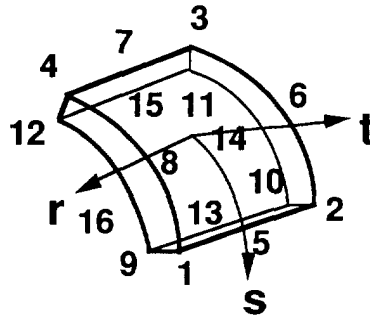
Fig. 4. A 16-node curvilinear side surface-parallel quadratic isoparametric cylindrical shell element.

$$^{t+\Delta t}\mathscr{R} = \int_{^{t-\Delta t}S} {}^{t+\Delta t}f_i^S \delta v_i^S \, {}^{t+\Delta t}\mathrm{d}S \tag{28}$$

where the $^{t+\Delta t}f_i^S$ is the surface force vectors applied on the surface S at time $t+\Delta t$, and $\delta_0 v_i^S$ is the i-th component of the incremental virtual displacement vector evaluated on the loaded surface. When the hydrostatic pressure is applied, the loading-path is always deformation-dependent and the load vector should be evaluated at the current configuration. The external virtual work can, however, be approximated to sufficient accuracy using the intensity of loading corresponding to time $t+\Delta t$, integrated over the surface area, $^{t+\Delta t}S^{(k-1)}$ calculated at the $(k-1)$th iteration as follows:

$$^{t+\Delta t}\mathscr{R} = \int_{^{t+\Delta t}S^{(k-1)}} {}^{t+\Delta t}f_i^S \delta_0 v_i^S \, {}^{t+\Delta t}\mathrm{d}S. \tag{29}$$

4. ISOPARAMETRIC FINITE ELEMENT DISCRETIZATION

In this section, a general nonlinear displacement-based finite element formulation is presented. The basic steps in the derivation of finite element equations are to select the interpolation functions of the displacements and element coordinates. Because the new element coordinates are obtained by adding the element displacements to the original coordinates in the incremental analysis, the same interpolations can be employed for the displacements and coordinates. In the present study, 16-node quadrilateral elements (Fig. 4) are employed because of their computational efficiency, as compared to their lower-order linear counterparts, which are too stiff to model the shear deformation of each lamina in the laminate.

The convected coordinates of a generic point (x, θ, z) in an element of the i-th layer with eight nodal points on each of the top and bottom surfaces are, in terms of the natural coordinates r, s, given by

$$x^{(i)}(r,s,z) = \left(1 - \frac{z}{h_i}\right) \sum_{k=1}^{8} \psi_k(r,s)_b x_k^{(i)} + \frac{z}{h_i} \sum_{k=1}^{8} \psi_k(r,s)_t x_k^{(i)} \tag{30a}$$

$$\theta^{(i)}(r,s,z) = \left(1 - \frac{z}{h_i}\right) \sum_{k=1}^{8} \psi_k(r,s)_b \theta_k^{(i)} + \frac{z}{h_i} \sum_{k=1}^{8} \psi_k(r,s)_t \theta_k^{(i)} \tag{30b}$$

$$z^{(i)}(r,s,z) = \left(1 - \frac{z}{h_i}\right) \sum_{k=1}^{8} \psi_k(r,s)_b z_k^{(i)} + \frac{z}{h_i} \sum_{k=1}^{8} \psi_k(r,s)_t z_k^{(i)} \tag{30c}$$

where $\psi_k(r,s)$ are the interpolation functions taking a value of unity at nodes k and zero at all other nodes. The quantities, $_b x_k^{(i)}$, $_b \theta_k^{(i)}$, $_b z_k^{(i)}$ and $_t x_k^{(i)}$, $_t \theta_k^{(i)}$, $_t z_k^{(i)}$ are coordinates of the nodal point k on the bottom and top surfaces of the i-th layer, respectively. In the layerwise linear displacement theory, the incremental displacements of the i-th lamina are given by

$$\{_0 \mathbf{v}^{(i)}\} = [T_{BT}^{(i)}(z)][\boldsymbol{\Phi}(r,s)]\{_0 \mathbf{V}_{BT}^{(i)}\} \tag{31}$$

in which $[T_{BT}^{(i)}]$ is the linear matrix operator

$$[T_{BT}^{(i)}(z)] = \begin{bmatrix} 1-\dfrac{z}{h_i} & 0 & 0 & \dfrac{z}{h_i} & 0 & 0 \\[2ex] 0 & 1-\dfrac{z}{h_i} & 0 & 0 & \dfrac{z}{h_i} & 0 \\[2ex] 0 & 0 & 1-\dfrac{z}{h_i} & 0 & 0 & \dfrac{z}{h_i} \end{bmatrix} \tag{32a}$$

while the nodal displacement vector $\{_0 \mathbf{V}_{BT}^{(i)}\}$ of the i-th layer is defined by

$$\{_0 \mathbf{V}_{BT}^{(i)}\}^T = \{_0 U_{b1}^{(i)} \cdots {}_0 U_{b8}^{(i)} {}_0 V_{b1}^{(i)} \cdots {}_0 V_{b8}^{(i)} {}_0 W_{b1}^{(i)} \cdots {}_0 W_{b8}^{(i)} {}_0 U_{t1}^{(i)} \cdots {}_0 U_{t8}^{(i)} {}_0 V_{t1}^{(i)} \cdots {}_0 V_{t8}^{(i)} {}_0 W_{t1}^{(i)} \cdots {}_0 W_{t8}^{(i)}\} \tag{32b}$$

and

$$[\boldsymbol{\Phi}(r,s)] = \begin{bmatrix} \{\psi\} & \{0\} & \{0\} & \{0\} & \{0\} & \{0\} \\ \{0\} & \{\psi\} & \{0\} & \{0\} & \{0\} & \{0\} \\ \{0\} & \{0\} & \{\psi\} & \{0\} & \{0\} & \{0\} \\ \{0\} & \{0\} & \{0\} & \{\psi\} & \{0\} & \{0\} \\ \{0\} & \{0\} & \{0\} & \{0\} & \{\psi\} & \{0\} \\ \{0\} & \{0\} & \{0\} & \{0\} & \{0\} & \{\psi\} \end{bmatrix} \tag{32c}$$

wherein

$$\{\psi\} = \{\psi_1 \quad \psi_2 \quad \psi_3 \quad \psi_4 \quad \psi_5 \quad \psi_6 \quad \psi_7 \quad \psi_8\} \tag{33}$$

and $\{0\}$ is 1×8 null matrix. $\psi_k(r,s)$, $k = 1, \ldots, 8$, are the same interpolation functions used in eqns (30).

The right hand side of eqn (25) can here be rewritten using the matrix differential operators, B_{LL}, B_{NL}, B_{NN} and $T_{BT}^{(i)}$ defined in the eqns (26), (27) and (32) as follows:

$$\int_{_0V} C_{ijrs} \, {}_0\bar{e}_{rs}^L \delta_0 \bar{e}_{ij}^L \, {}^0 \mathrm{d}V + \int_{_0V} C_{ijrs} \, {}_0\bar{e}_{rs}^N \delta_0 \bar{e}_{ij}^L \, {}^0 \mathrm{d}V + \int_{_0V} C_{ijrs} \, {}_0\bar{e}_{rs}^L \delta_0 \bar{e}_{ij}^N \, {}^0 \mathrm{d}V$$

$$+ \int_{_0V} C_{ijrs} \, {}_0\bar{e}_{rs}^N \delta_0 \bar{e}_{ij}^N \, {}^0 \mathrm{d}V + \int_{_0V} \delta\hat{\eta}_{ki} \, {}_0^t \hat{S}_{ij} \hat{\eta}_{kj} \, {}^0 \mathrm{d}V + \int_{_0V} {}_0^t \bar{S}_{ij} \{\delta_0 \bar{e}_{ij}^L + \delta_0 \bar{e}_{ij}^N\} \, {}^0 \mathrm{d}V$$

$$= \int_{_0S} \sum_{k=1}^{NS} \int_{h_{k-1}}^{h_k} \delta\{_0 \mathbf{V}_{BT}^{(k)}\}^T ([B_{LL}^{(k)}][T_{BT}^{(k)}][\boldsymbol{\Phi}])^T [\bar{Q}^{(k)}][B_{LL}^{(k)}][T_{BT}^{(k)}][\boldsymbol{\Phi}]\{_0 \mathbf{V}_{BT}^{(k)}\} \rho^{(k)} \, \mathrm{d}z \, \mathrm{d}\theta \, \mathrm{d}x$$

$$+ \int_{_0S} \sum_{k=1}^{NS} \int_{h_{k-1}}^{h_k} \delta\{_0 \mathbf{V}_{BT}^{(k)}\}^T ([B_{NL}^{(k)}][T_{BT}^{(k)}][\boldsymbol{\Phi}])^T [\bar{Q}^{(k)}][B_{LL}^{(k)}][T_{BT}^{(k)}][\boldsymbol{\Phi}]\{_0 \mathbf{V}_{BT}^{(k)}\} \rho^{(k)} \, \mathrm{d}z \, \mathrm{d}\theta \, \mathrm{d}x$$

$$+ \int_{_0S} \sum_{k=1}^{NS} \int_{h_{k-1}}^{h_k} \delta\{_0 \mathbf{V}_{BT}^{(k)}\}^T ([B_{LL}^{(k)}][T_{BT}^{(k)}][\boldsymbol{\Phi}])^T [\bar{Q}^{(k)}][B_{NL}^{(k)}][T_{BT}^{(k)}][\boldsymbol{\Phi}]\{_0 \mathbf{V}_{BT}^{(k)}\} \rho^{(k)} \, \mathrm{d}z \, \mathrm{d}\theta \, \mathrm{d}x$$

$$+ \int_{_0S} \sum_{k=1}^{NS} \int_{h_{k-1}}^{h_k} \delta\{_0 \mathbf{V}_{BT}^{(k)}\}^T ([B_{NL}^{(k)}][T_{BT}^{(k)}][\boldsymbol{\Phi}])^T [\bar{Q}^{(k)}][B_{NL}^{(k)}][T_{BT}^{(k)}][\boldsymbol{\Phi}]\{_0 \mathbf{V}_{BT}^{(k)}\} \rho^{(k)} \, \mathrm{d}z \, \mathrm{d}\theta \, \mathrm{d}x$$

$$+ \int_{0^S} \sum_{k=1}^{NS} \int_{h_{k-1}}^{h_k} \delta\{_0^t V_{BT}^{(k)}\}^T ([B_{NN}^{(k)}][T_{BT}^{(k)}][\Phi])^T [_0^t \hat{S}^{(k)}][B_{NN}^{(k)}][T_{BT}^{(k)}][\Phi]\{_0^t V_{BT}^{(k)}\}\rho^{(k)} \, dz \, d\theta \, dx$$

$$+ \int_{0^S} \sum_{k=1}^{NS} \int_{h_{k-1}}^{h_k} \delta\{_0^t V_{BT}^{(k)}\}^T ([B_{LL}^{(k)}][T_{BT}^{(k)}][\Phi])^T [_0^t \bar{S}^{(k)}]\rho^{(k)} \, dz \, d\theta \, dx$$

$$+ \int_{0^S} \sum_{k=1}^{NS} \int_{h_{k-1}}^{h_k} \delta\{_0^t V_{BT}^{(k)}\}^T ([B_{NL}^{(k)}][T_{BT}^{(k)}][\Phi])^T [_0^t \bar{S}^{(k)}]\rho^{(k)} \, dz \, d\theta \, dx \tag{34}$$

in which

$$[_0^t \hat{S}_{ij}] = \begin{bmatrix} [_0^t S'] & [0] & [0] \\ [0] & [_0^t S'] & [0] \\ [0] & [0] & [_0^t S'] \end{bmatrix} \tag{35}$$

with

$$[_0^t S'] = \begin{bmatrix} _0^t S_{xx} & _0^t S_{x\theta} & _0^t S_{x\zeta} \\ _0^t S_{x\theta} & _0^t S_{\theta\theta} & _0^t S_{\zeta\theta} \\ _0^t S_{x\zeta} & _0^t S_{\theta\zeta} & _0^t S_{\zeta\zeta} \end{bmatrix} \tag{36}$$

and

$$\{_0^t \bar{S}_{ij}\}^T = \{_0^t S_{xx} \; _0^t S_{\theta\theta} \; _0^t S_{zz} \; _0^t S_{\theta z} \; _0^t S_{xz} \; _0^t S_{x\theta}\}. \tag{37}$$

Similar operations on eqn (29) yield the following

$$\int_{t+\Delta t_S(k-1)} {}^{t+\Delta t} f_i^S \delta_0 v_i^S {}^{t+\Delta t} dS = \int_S \delta\{_0 V_{BT}^{(NS)}\}^T ([T_{BT}^{(NS)}][\Phi])^T \{n^{(NS+1)}\}p\rho^{(NS-1)} \, dx \, d\theta. \tag{38}$$

On computing the right hand sides of eqns (34) and (38) as sums of integrations over the volume and areas of all finite elements, followed by equating them, and incorporating the boundary conditions, the principle of virtual displacement is invoked to obtain the incremental equations of motion as follows:

$$[K_L]\{_0 V\} + [K_N]\{_0 V\} = \{f_L\} - \{f_N\} \tag{39}$$

where

$$[K_L] \equiv \sum_{m=1}^{NL} \sum_{k=1}^{NS} \int_{S^{(m)}} \int_{h_{k-1}}^{h_k} ([B_{LL}^{(k)}][T_{BT}^{(k)}][\Phi])^T [\bar{Q}^{(k)}][B_{LL}^{(k)}][T_{BT}^{(k)}][\Phi]\rho^{(k)} \, dz \, dS \tag{40a}$$

$$[K_N] \equiv \sum_{m=1}^{NL} \sum_{k=1}^{NS} \int_{S^{(m)}} \int_{h_{k-1}}^{h_k} 2([B_{LL}^{(k)}][T_{BT}^{(k)}][\Phi])^T [\bar{Q}^{(k)}][B_{NL}^{(k)}][T_{BT}^{(k)}][\Phi]\rho^{(k)} \, dz \, dS$$

$$+ \sum_{m=1}^{NL} \sum_{k=1}^{NS} \int_{S^{(m)}} \int_{h_{k-1}}^{h_k} ([B_{NL}^{(k)}][T_{BT}^{(k)}][\Phi])^T [\bar{Q}^{(k)}][B_{NL}^{(k)}][T_{BT}^{(k)}][\Phi]\rho^{(k)} \, dz \, dS$$

$$+ \sum_{m=1}^{NL} \sum_{k=1}^{NS} \int_{S^{(m)}} \int_{h_{k-1}}^{h_k} ([B_{NN}^{(k)}][T_{BT}^{(k)}][\Phi])^T [_0^t \hat{S}^{(k)}][B_{NN}^{(k)}][T_{BT}^{(k)}][\Phi]\rho^{(k)} \, dz \, dS \tag{40b}$$

$$\{f_L\} \equiv \sum_{m=1}^{NT} \int_{S^{(m)}} [[T_{BT}^{(NS)}][\Phi]]^T \{n^{(NS+1)}\}p\rho^{(NS+1)} \, dS \tag{41a}$$

$$\{\mathbf{f_N}\} = \sum_{m=1}^{NL} \sum_{k=1}^{NS} \int_{S^{(m)}} \int_{h_{k-1}}^{h_k} ([B_{LL}^{(k)}][T_{BT}^{(k)}][\Phi])^T[{}_0^t\bar{S}^{(k)}]\rho^{(k)} \, \mathrm{d}z \, \mathrm{d}S$$

$$+ \sum_{m=1}^{NL} \sum_{k=1}^{NS} \int_{S^{(m)}} \int_{h_{k-1}}^{h_k} ([B_{NL}^{(k)}][T_{BT}^{(k)}][\Phi])^T[{}_0^t\bar{S}^{(k)}]\rho^{(k)} \, \mathrm{d}z \, \mathrm{d}S \qquad (41\mathrm{b})$$

with $\mathrm{d}S = \mathrm{d}x \, \mathrm{d}\theta$

and

$$\{{}_0\mathbf{V}\}^T = \{{}_0U_{b1}^{(1)} \cdots {}_0U_{b8}^{(1)} \, {}_0V_{b1}^{(1)} \cdots {}_0V_{b8}^{(1)} \, {}_0W_{b1}^{(1)} \cdots {}_0W_{b8}^{(1)} \, {}_0U_{t1}^{(1)}$$

$$\cdots {}_0U_{t8}^{(1)} \, {}_0V_{t1}^{(1)} \cdots {}_0V_{t8}^{(1)} \, {}_0W_{t1}^{(1)} \cdots {}_0W_{t8}^{(1)} \, {}_0U_{b1}^{(i)} \cdots {}_0U_{b8}^{(i)} \, {}_0V_{b1}^{(i)} \cdots {}_0V_{b8}^{(i)} \, {}_0W_{b1}^{(i)}$$

$$\cdots {}_0W_{b8}^{(i)} \, {}_0U_{t1}^{(i)} \cdots {}_0U_{t8}^{(i)} \, {}_0V_{t1}^{(i)} \cdots {}_0V_{t8}^{(i)} \, {}_0W_{t1}^{(i)} \cdots {}_0W_{t8}^{(i)} \, {}_0U_{b1}^{(N)} \cdots {}_0U_{b8}^{(N)} \, {}_0V_{b1}^{(N)}$$

$$\cdots {}_0V_{b8}^{(N)} \, {}_0W_{b1}^{(N)} \cdots {}_0W_{b8}^{(N)} \, {}_0U_{t1}^{(N)} \cdots {}_0U_{t8}^{(N)} \, {}_0V_{t1}^{(N)} \cdots {}_0V_{t8}^{(N)} \, {}_0W_{t1}^{(N)} \cdots {}_0W_{t8}^{(N)}\}. \qquad (42)$$

5. ITERATIVE SOLUTION STRATEGY

Because the nodal point forces at time $t + \Delta t$ depend nonlinearly on the nodal point displacements, it is necessary to iterate for obtaining a reasonably accurate solution of eqn (39). The most frequently used iteration scheme for solutions of nonlinear finite element equations is the Newton–Raphson iteration because reformations and triangularizations of stiffness matrices at selective load and iteration steps are less expensive in terms of computer time. In the Newton–Raphson method, only the stress force vector [see eqn (39)] is modified without changing the stiffness matrix after each iteration of a certain load step and the following algorithm for eqn (39) is developed.

$$([K_L] + {}^t[K_N])\{{}_0\mathbf{V}\}^{(i)} = {}^{t+\Delta t}\{f_L\} - {}^{t+\Delta t}\{f_N\}^{(i-1)} \qquad (43)$$

$$^{t+\Delta t}\{\mathbf{V}\}^{(i)} = {}^{t+\Delta t}\{\mathbf{V}\}^{(i-1)} + [A]^{(i)}\{{}_0\mathbf{V}\}^{(i)} \qquad (44)$$

with the initial conditions $^{t+\Delta t}\{f_N\}^{(0)} = {}^t\{f_N\}$, and $^{t+\Delta t}\{\mathbf{V}\}^{(0)} = {}^t\{\mathbf{V}\}$, where the index i means the number of iterations performed in a certain time step t; the subscripts L and N denote the linear and nonlinear components evaluated at time t, and the diagonal matrix $[A]$ is the Aitken acceleration factor to increase the convergence rate. Equation (43) is equivalent to eqn (39). Furthermore, in the computer program, the process of the assemblage for the total stiffness matrix can be divided into two groups: the first group contains linear elements where stiffness matrices of each individual element are only calculated at the first load step and remain unchanged during the whole loading process. The second one refers to the nonlinear elements where nonlinear stiffness matrices of the element can be evaluated at the first iteration of each load step with nonlinear force vectors, at each iteration of every load step using the contributions of current displacements or stresses. The applied force and the stress force vectors [i.e. $^{t+\Delta t}\{f_L\}$ and $^{t+\Delta t}\{f_N\}^{(i-1)}$ in eqn (43)] are calculated according to eqns (41) as follows:

$$^{t+\Delta t}\{f_L\} = \sum_{m=1}^{NT} \int_{S^{(m)}} [[{}^{t-\Delta t}T_{BT}^{(NS)}][\Phi]]^T\{{}^{t+\Delta t}\mathbf{n}^{(NS+1)}\}p\rho^{(NS+1)} \, \mathrm{d}^{t+\Delta t}S \qquad (45)$$

and

$$^{t+\Delta t}\{f_N\}^{(i-1)} = \sum_{m=1}^{NL} \int_{S^{(m)}} \sum_{k=1}^{NS} \int_{h_{k-1}}^{h_k} ([^{t+\Delta t}B_{LL}^{(k)}]^{(i-1)}[^{t+\Delta t}T_{BT}^{(k)}]^{(i-1)}[\Phi])^T[_0^{t+\Delta t}\bar{S}^{(k)}]^{(i-1)}\rho^{(k)} \, dz \, _0^{t+\Delta t}dS$$

$$+ \sum_{m=1}^{NL} \int_{S^{(m)}} \sum_{k=1}^{NS} \int_{h_{k-1}}^{h_k} ([^{t+\Delta t}B_{NL}^{(k)}]^{(i-1)}[^{t+\Delta t}T_{BT}^{(k)}]^{(i-1)}[\Phi])^T[_0^{t+\Delta t}\bar{S}^{(k)}]^{(i-1)}\rho^{(k)} \, dz \, _0^{t+\Delta t}dS \qquad (46)$$

where

$$[^{t+\Delta t}B_{LL}^{(k)}]^{(i-1)}[^{t-\Delta t}T_{BT}^{(k)}]^{(i-1)}:$$

linear differential operator of the k-th layer evaluated at $(i-1)$th iteration of each load step.

$$[^{t+\Delta t}B_{NL}^{(k)}]^{(i-1)}[^{t+\Delta t}T_{BT}^{(k)}]^{(i-1)}:$$

nonlinear differential operator of the k-th layer evaluated at $(i-1)$th iteration of each load step.

It may be noted here that normal direction vectors and differential area of the loaded surface reduce to a constant value evaluated at the first iteration of the first load step when the constant directional load is applied. The 6×1 element stress vector $\{_0^{t+\Delta t}\bar{S}^{(k)}\}^{(i-1)}$ can be calculated by generalizing the linear elastic relations, $\{_0^{t+\Delta t}\bar{S}^{(k)}\}^{(i-1)} = \bar{Q}_{ij}^{(k)}\{_0^{t+\Delta t}\bar{\epsilon}^{(k)}\}^{(i-1)}$ (Hooke's law in infinitesimal displacement conditions) for the linear material because the second Piola–Kirchhoff stress and Green–Lagrangian strain tensors are invariant under rigid body motions in large displacement and rotation. The same procedure can be applied to evaluate the 9×9 element stress matrix $[_0^t\hat{S}^{(k)}]$ that appears in the nonlinear stiffness matrix of eqn (40b).

In actual computer programming, the active columns and addresses of the diagonal elements of the total stiffness matrix are stored effectively in a one-dimensional array and an effective subroutine COLSOL (active column solver) is used to finally obtain the incremental displacement for the unbalanced force, $^{t+\Delta t}\Delta R^{(i-1)} = ^{t+\Delta t}\{f_L\} - ^{t+\Delta t}\{f_N\}^{(i-1)}$ in the $(i-1)$th iteration. The iteration is continued until the out-of-balance load vector and the displacement increments are sufficiently small, i.e. the iteration scheme is terminated at the current load step and moves to the next load step, when the force convergence criterion,

$$\frac{\|^{t+\Delta t}\{f_L\} - ^{t+\Delta t}\{f_N\}^{(i)}\|}{\|^{t+\Delta t}\{f_L\} - ^t\{f_L\}\|} < \varepsilon_f \qquad (47a)$$

and the energy convergence criterion,

$$\frac{\{_0V\}^{(i)T}(^{t+\Delta t}\{f_L\} - ^{t+\Delta t}\{f_N\}^{(i-1)})}{\{_0V\}^{(1)T}(^{t+\Delta t}\{f_L\} - ^t\{f_L\})} < \varepsilon_e \qquad (47b)$$

are simultaneously satisfied, where ε_f and ε_e are preset force and energy tolerances, and $\|\cdot\|$ denotes the Euclidean norm of the column vector. The Newton–Raphson method with a large value of the load increment requires a number of iterations in the nonlinear regime; it may introduce serious errors and, indeed, diverge from the exact solution. Therefore, a rather small load increment would be necessary in the nonlinear regime. It may, however, be noted that the larger value of load increment is recommended, with a specific accuracy, for the linear regime, in the interest of computational efficiency.

The prediction of nonlinear structural behavior by the Newton–Raphson method is successfully achieved before the critical (limit) point of the solution, because the residual force vector and the gradient of the total system matrix do not change in sign drastically; i.e. physically, the total stiffness matrix monotonically decreases in the present investigation as the applied load is increased up to the limit load. In practice, during the solution process of the system, the stiffness matrix may approach singularity at the critical point and the

Newton-type method generally fails to give satisfactory results because of the multiple admissible solutions for a single value of load. It is necessary to modify the standard form of the Newton-type method if it is employed to trace the postbuckling solution. The technique necessary to modify this method, based on displacement increment, is therefore employed beyond the critical (limit) point, which is shown to be efficient and reliable. In the event of a displacement increment $_0V_q$ being specified at the load step, $t + \Delta t$, instead of varying the load parameter, the q-th component of the total displacement vector at the first iteration of the time step $t + \Delta t$, is incremented by $_0V_q$ and the initial solution vector $^{t+\Delta t}V^{(0)}$ is redefined as

$$^{t+\Delta t}\{V\}^{(0)} = {}^{t}\{V\} \; ; \quad {}^{t+\Delta t}\lambda^{(0)} = {}^{t}\lambda \tag{48}$$

where the q-th component of the total displacement at time $t + \Delta t$, $^{t+\Delta t}V_q^{(0)} = {}^{t}V_q + {}_0V_q$ and the scalar quantity $^{t+\Delta t}\lambda^{(0)}$ is the initial load level that is calculated at the previous time step. The Newton–Raphson method introduced in calculating prebuckling solution is employed to obtain the unknown incremental displacement vector and the corresponding force vector with $_0V_q$ considered as fixed during iteration. The modified algorithm (see Batoz et al., 1976; Batoz and Dhatt, 1979) of eqn (39) becomes

$$([K_L] + {}^{t}[K_N])^{(i)} \{_0R\}^{(i)} = {}^{t-\Delta t}\{f_N\}^{(i-1)} \tag{49a}$$

$$([K_L] + {}^{t}[K_N])^{(i)} \{_0Q\}^{(i)} = {}^{t-\Delta t}\{f_L\} \tag{49b}$$

where $^{t+\Delta t}\{f_N\}^{(i-1)}$ is the residual vector (i.e. nonlinear force vector) evaluated at the $(i-1)$th iteration of the time step, $t + \Delta t$ and the $^{t-\Delta t}\{f_L\}$ is the applied load vector that is assumed to be proportional for each time step, which is multiplied by $_0\lambda^{(i)}$ to obtain the actual load corresponding to the prescribed displacement. The quantities $\{_0R\}^{(i)}$ and $\{_0Q\}^{(i)}$ are incremental displacements due to the residual force vector and the applied load vector, respectively. The complete solution of eqn (39) is now defined by

$$^{t+\Delta t}\{V\}^{(i)} = {}^{t+\Delta t}\{V\}^{(i-1)} + \{_0V\}^{(i)} \tag{50a}$$

$$\{_0V\}^{(i)} = \{_0R\}^{(i)} + {}_0\lambda^{(i)}\{_0Q\}^{(i)}. \tag{50b}$$

The value of incremental load scale factor, $_0\lambda^{(i)}$ can be obtained as follows, reflecting that the q-th component of the incremental displacement, i.e. $_0V_q^{(i)}$ is set to zero during iteration:

$$_0\lambda^{(i)} = -\frac{_0R_q^{(i)}}{_0Q_q^{(i)}} \tag{51}$$

where $R_q^{(i)}$ and $Q_q^{(i)}$ are the q-th components of vector $\{_0R\}^{(i)}$ and $\{_0Q\}^{(i)}$. In the present investigation, the total stiffness matrix of eqn (51) is not calculated at each iteration, but calculated and factorized at each time step. It is implicitly assumed that the total stiffness matrix remains non-singular at any solution level. Theoretically, if a certain displacement solution corresponds to a critical or singular point, the total stiffness matrix will be singular. However, in practice, it is impossible to obtain a solution vector exactly corresponding to a singular point, due to a large number of components of $^{t+\Delta t}\{V\}^{(i)}$ and possible round-off errors. The above-mentioned algorithm for solving eqns (49) is, therefore, utilized in this investigation without the problem of singularity of the total stiffness matrix encountered. In a situation where the matrix is singular, the previous algorithm should be modified to avoid the singularity in a manner suggested by Zienkiewicz (1971), and Thomas and Gallagher (1975). Furthermore, neither the stiffness matrix need be reorganized into partitioned form nor the sky-line and bandwidth of the stiffness matrix should be destroyed in the present investigation. Only two different load vectors [i.e. $^{t+\Delta t}\{f_N\}^{(i-1)}$ and $^{t+\Delta t}\{f_L\}$ in
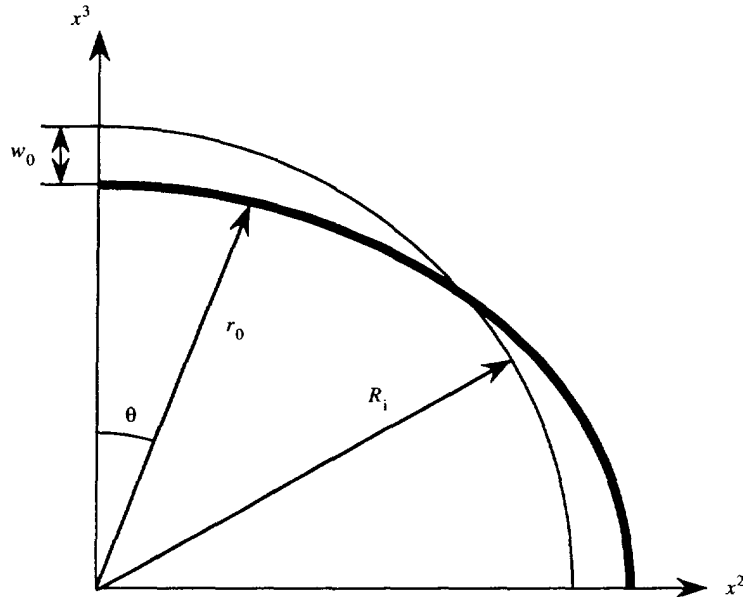
Fig. 5. Shape of a cylinder with modal imperfections.

eqn (49)] are involved, which are back-substituted in the subroutine COLSOL to calculate the incremental displacements simultaneously.

6. RESULTS AND DISCUSSION

First, the issues of validity of the present LLDT based nonlinear incremental formulation (developed earlier), the accuracy of the resulting special purpose nonlinear finite element code, and assessment of the convergence characteristics of the present 16 node layer element are addressed for shallow homogeneous isotropic and cross-ply [0/90] panels in the absence of imperfections. Also addressed is the issue of accuracy of the von-Karman nonlinear strain assumption which has been found to overestimate transverse displacements in the advanced nonlinear regime. The results of these studies are available in Hsia and Chaudhuri (in press), Kim and Chaudhuri (1995), and Chaudhuri and Hsia (to be published), and hence will not be presented here in the interest of brevity.

This study addresses the problem of nonlinear postbuckling behavior of an infinitely long thick symmetrically laminated cross-ply [90/0/90] cylinder. Double symmetry conditions permit every model under consideration to be limited to only a quarter of the geometry such that the corresponding surface-parallel displacements vanish along the center lines and the buckled shapes are assumed to be symmetric. As a result, a cylinder geometry with plane strain constraint has been chosen in the present investigation, which has, in the absence of any geometric imperfection, an inner surface radius R_i and thickness, h. In order to investigate a localization of the buckling pattern, a modal imperfection (mode 2 of classical buckling of a ring), given by

$$r_0(\theta) = R_i - w_0 \cos(2\theta) \tag{52a}$$

is introduced (Fig. 5). The radius of curvature of inner (bottom) surface of the innermost layer, $\rho^{(1)}$, and the corresponding surface metric, g_2, can be obtained as follows (see Kim and Chaudhuri, to be published):

$$g_2^{(1)} = \rho^{(1)} \approx \frac{R_i - 3w_0 \cos(2\theta)}{R_i + 3w_0 \cos(2\theta)} \tag{52b}$$

wherein terms $\mathcal{O}(w_0^2)$ and higher are neglected in both the numerator and denominator.

Layer 1
Layer 2
Layer 3
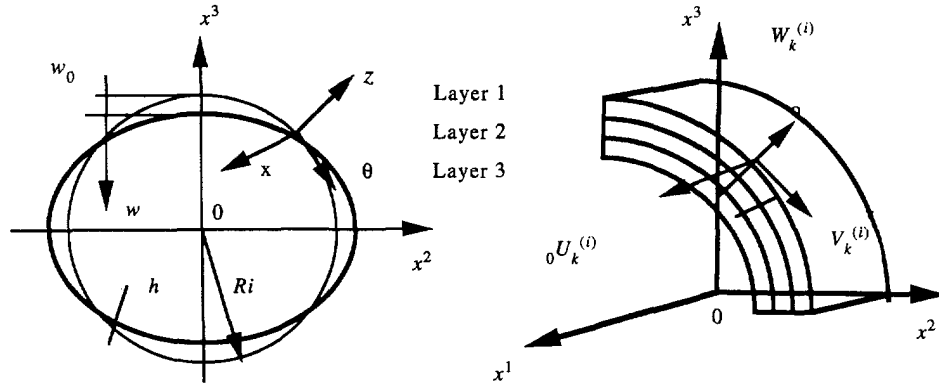
$NL = 10$
$NS = 3$

Geometric properties :

$Ri = 3.5$ in. $L = 0.534$ in.

$Ri/h = 3.0, 6.0, 8.0, 12.0, 18.0, 30.0, 60.0$

$w_0/Ri = 0.005$ and $c = 1.0$

Fig. 6. Nomenclature and property definitions for the long cylinder buckling problem.

Table 1. Material data with respect to the global coordinate $(x\,\theta, \zeta)$ for different layup

Layup	E_{xx}	$E_{\theta\theta}$	E_{zz}	$G_{x\theta}$	G_{xz}	$G_{\theta z}$
$\alpha = 0^*$	E_{LL}	E_{TT}	E_{TT}	G_{LT}	G_{LT}	G_{TT}
$\alpha = 90^*$	E_{TT}	E_{LL}	E_{TT}	G_{LT}	G_{TT}	G_{LT}

Material properties: $E_{LL} = 18.0$ Msi, $E_{TT} = 1.55$ Msi, $v_{LT} = 0.575$, $G_{LT} = 0.85$ Msi, $G_{TT} = 0.45$ Msi.

The laminated cylindrical shell geometry with imperfections, and material properties are described in Fig. 6 and Table 1, respectively. The finite element model of a quarter of the plane strain ring along with the prescribed boundary conditions is presented in Fig. 7. Because the loading and geometric symmetries are assumed, boundary conditions on the surfaces in Fig. 7 can be prescribed as follows:

Geometric symmetry

on the surfaces ABFE and CDHG; $\quad _0v(x, 0, \zeta) = 0 \quad$ and $\quad _0v(x, \pi/2, \zeta) = 0 \quad$ (53a)

on the surface EHGF; $\quad _0u(0, \theta, \zeta) = 0.$ (53b)

Loading symmetry

Traction force on the surface BCGF; $\quad f_i^S = P_r(x, \theta, \rho^{(NS)})n_i^{(NS)}.$ (54)

The plane strain condition in the three-dimensional model is obtained by applying the displacement constraints as shown below:

$$_0u_k^{(i)} = 0, \quad k = 1, \ldots, 16$$ (55a)

$$_0v_1^{(i)} = {}_0v_2^{(i)} = {}_0v_5^{(i)}; \quad _0v_9^{(i)} = {}_0v_{10}^{(i)} = {}_0v_{13}^{(i)}; \quad _0v_3^{(i)} = {}_0v_4^{(i)} = {}_0v_7^{(i)}; \quad _0v_{11}^{(i)} = {}_0v_{12}^{(i)} = {}_0v_{15}^{(i)};$$

$$_0v_6^{(i)} = {}_0v_8^{(i)}; \quad _0v_{14}^{(i)} = {}_0v_{16}^{(i)}$$ (55b)
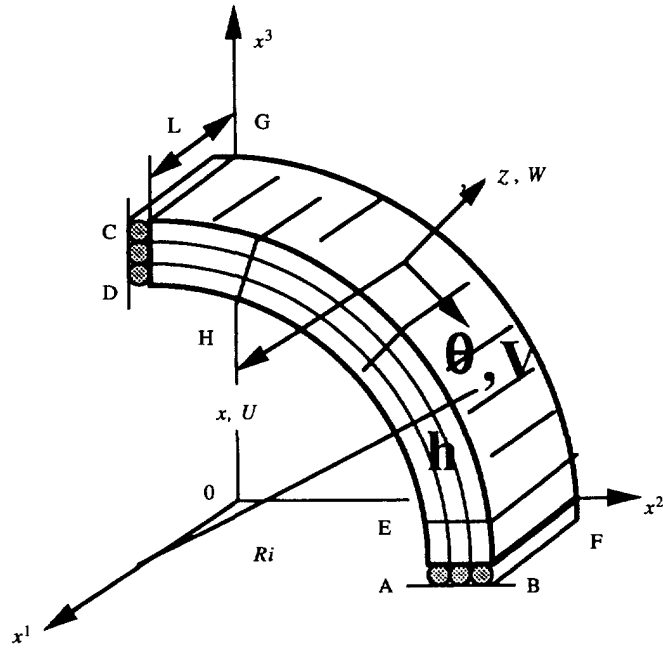
Surface ABCD and EFGH : $U = 0$

Surface ABFE and CDHG : $V = 0$

Fig. 7. Finite element model of multilayered composite plane strain cylinder/ring.

Table 2. Comparison of buckling hydrostatic pressures for a perfect composite $[90/0/90]$ long cylinder ($R_i = 3.5$ in., $w_0/R_i = 0$)

Radius to thickness ratio R_i/h	Buckling pressure, P_{cr} (psi)	
	Present investigation	Donnel-type
3.0	59500.0	112202.40
6.0	14900.0(21300.0)*	17615.50
8.0	8750.0	9459.87
12.0	2500.0	2484.72
18.0	812.0	767.23
30.0	187.0	171.42
60.0	26.5	21.97

*The quantity in parenthesis corresponds to buckling pressure computed neglecting transverse shear deformation, the value of which is 16% higher than Donnell-type buckling pressure.

$$_0w_1^{(i)} = {}_0w_2^{(i)} = {}_0w_5^{(i)} ; \quad _0w_9^{(i)} = {}_0w_{10}^{(i)} = {}_0w_{13}^{(i)} ; \quad _0w_3^{(i)} = {}_0w_4^{(i)} = {}_0w_7^{(i)} ;$$

$$_0w_{11}^{(i)} = {}_0w_{12}^{(i)} = {}_0w_{15}^{(i)} ; \quad _0w_6^{(i)} = {}_0w_8^{(i)} ; \quad _0w_{14}^{(i)} = {}_0w_{16}^{(i)} \quad (55c)$$

where the superscript, i, denotes element number. Additionally, the corresponding CLT-based solution is obtained by adopting the following material constraints:

$$G_{\theta z} = E_m/[2(1+v_m)] ; \quad G_{x\theta} = G_{xz} = 1000 \times G_{\theta z}. \quad (56)$$

A comparison of the present buckling results with the available Donnell-type linearized buckling pressure, given by Jones and Morgan (1975),

$$p_{cr} = 3.0 \times \left(D_{22} - \frac{B_{22}^2}{A_{22}} \right) / R_m^3 \quad (57)$$

is presented in Table 2, where R_m is the mean radius of the cylinder and A_{22}, B_{22} and D_{22}
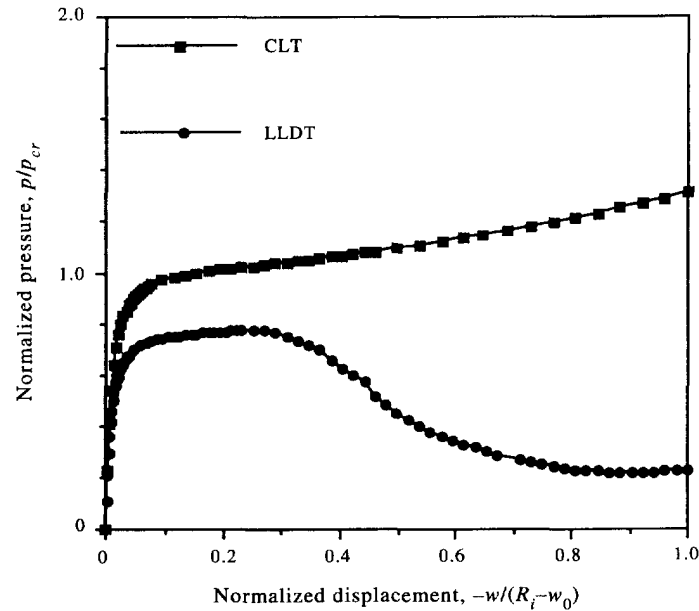
Fig. 8. Equilibrium paths for a thick-section composite cylinder [90/0/90] computed using CLT and
LSDT ($R_i/h = 6.0$, $w_0 = 0.005*R_i$).

represent the extensional, bending extension coupling, and bending stiffness of the cylinder
in the circumferential direction, respectively. The Donnell-type differential equations can
be obtained by neglecting the transverse shear deformations, the prebuckling deformation
and the effect of gradients of the circumferential displacement, v along x and θ directions
on the curvature, which can be subsequently presented in terms of variations of assumed
displacements, u, v and w just after onset of buckling. The solution is a simple closed form
buckling criterion applicable for external (hydrostatic) pressure, p. The present hydrostatic
buckling pressures are somewhat higher than their Donnell-type counterparts in the very
thin case, because the latter does not take into account the membrane action due
to curvature effect. However, the difference between the present buckling pressure and
Donnell-type buckling pressure decreases with the increase of the radius to thickness
ratio, because the transverse shear effect compensates for the aforementioned error as
seen in Table 2.

Figure 8 shows a comparison of the normalized pressure vs normalized displacements,
$w^* = -w/(R_i - w_0)$ at $\theta = 0°$ plots, computed using the classical lamination theory (CLT)
and the present theory, for a symmetrically laminated [90/0/90] cylinder. It can be seen here
that a stable postbuckling solution that is associated with the periodicity of the classical or
modal buckling patterns is obtained when the CLT is used. However, in contrast to the
CLT solution, a limit point appears on the postbuckling path computed using the LLDT,
even in the linear elastic material case, which results in significant reduction of the maximum
pressure by 21.7% of the CLT based linearized buckling load. It may be noted that because
the structure cannot follow an unstable equilibrium path, it will switch to a localization
mode with a significant drop of the load carrying capacity of the composite [90/0/90]
cylindrical shell under investigation. In analogy to phase transition phenomena such as
condensation of gases, the melting of solids, phenomena of ferromagnetism and anti-
ferromagnetism, the famous family of lambda-transitions—e.g. order-disorder transitions
in alloys, the transition from liquid He I to liquid He II (superfluidity of liquid helium at
low temperatures) or the transition from a normal to a superconducting material (super-
conductivity of metal at low temperatures) and so on (Pathria, 1977) studied in condensed
matter physics, this represents a long range order (of nonlocal or gage theories) that is
intimately connected with spontaneous symmetry breaking. For example, there is a long
range order in the ferromagnet—all the spins are lined up in the same direction, resulting
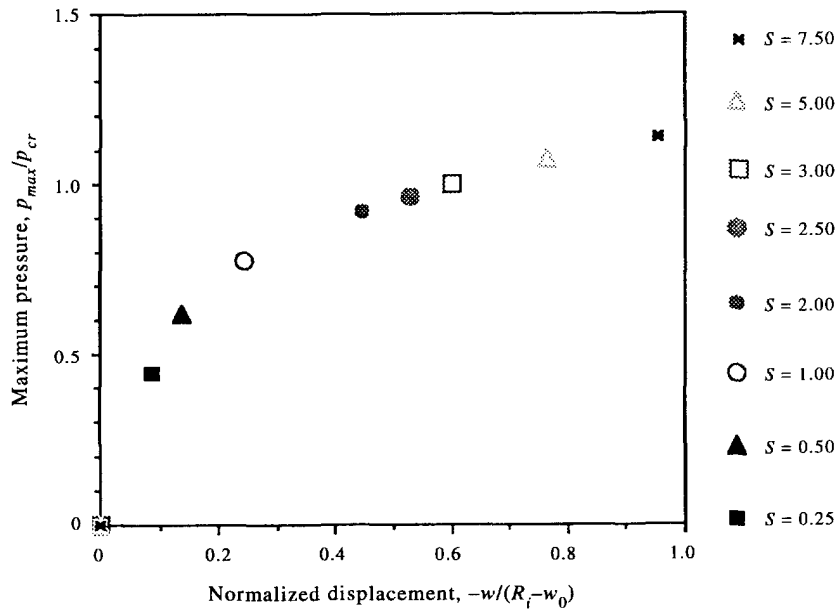
Fig. 9. Normalized maximum pressure vs displacement of composite [90/0/90] cylinder $(R_i/h = 6.0, w_0 = 0.005*R_i)$ for different shear modulus ratios.

in spontaneous breaking of rotational invariance (Zee, 1995). In the example problem studied here, localization of the deformation pattern is associated with spontaneous breaking of the periodicity of classical or modal buckling patterns.

In order to investigate the transverse shear effect on the limit point load, numerical results for different shear modulus values, G^*_{LT}, are presented in Fig. 9. The same radius to thickness ratio (i.e. $R_i/h = 6$), and the modal imperfection (i.e. $w_0 = 0.005*R_i$) are maintained in this plot, while varying the value of s defined by $s = G^*_{LT}/G_{LT}$, where G^*_{LT} is the modified shear modulus. As the value of s increases, the effect of transverse shear deformation diminishes, which reduces the present solution to its CLT based counterpart. These results lead to the conclusion that the CLT is not suitable for obtaining an accurate load–displacement solution for a composite cylinder with low shear modulus to Young's modulus ratio, which characterizes the carbon fiber reinforced composites.

The computed deformed shapes of a thick composite [90/0/90] cylindrical shell $(R_i/h = 6, w_0 = 0.005*R_i)$ in the radial direction are shown in Fig. 10(a–d) for four different displacements and the corresponding hydrostatic pressures (where the normalization with respect to the classical buckling pressure of the perfect cylinder, p_{cr}, is used). At the initial stage of loading, the maximum transverse deflection variation with the increase of load occurs around $\theta = 0^\circ$, while the corresponding nodal (no deflection) line of the deformed shape is maintained at $\theta = 90^\circ$ [Fig. 10(a)] in the case of the thick cylindrical shell under investigation, which is in marked contrast with what happens in the case of a thin cylindrical shell, where the nodal line is located at $\theta = 45^\circ$ (not shown here). This result implies that the thick [90/0/90] cylindrical shell is susceptible to deform locally even in the presence of a modal imperfection, e.g. out-of-roundedness. As the maximum pressure is reached, the nodal line travels from $\theta = 90^\circ$ up to $\theta = 50^\circ$, while the transverse deflection at $\theta = 90^\circ$ starts to increase slightly with the increase of the load as shown in Fig. 10(b,c). Finally, as the load drops beyond the limit point, the nodal line does not move any further and the sections, $\theta = 0^\circ$ and $\theta = 90^\circ$ deflect in the opposite directions up to the ultimate point of the load–displacement plot as shown in Fig. 10(d).

Figure 11 shows a plot of the load parameter normalized by classical buckling pressure of the perfect cylinder, p_{cr}, vs the normalized displacement with modal imperfection $w_0 = 0.005*R_i$ when the radius to thickness ratio increases. It is noteworthy that the limit point is delayed as the radius to thickness ratio increases (i.e. as the effect of interlaminar shear/normal deformation decreases), and finally disappears in the very thin cylinder case $(R_i/h = 60$ and beyond), which is to be expected in accordance with the CLT. The latter
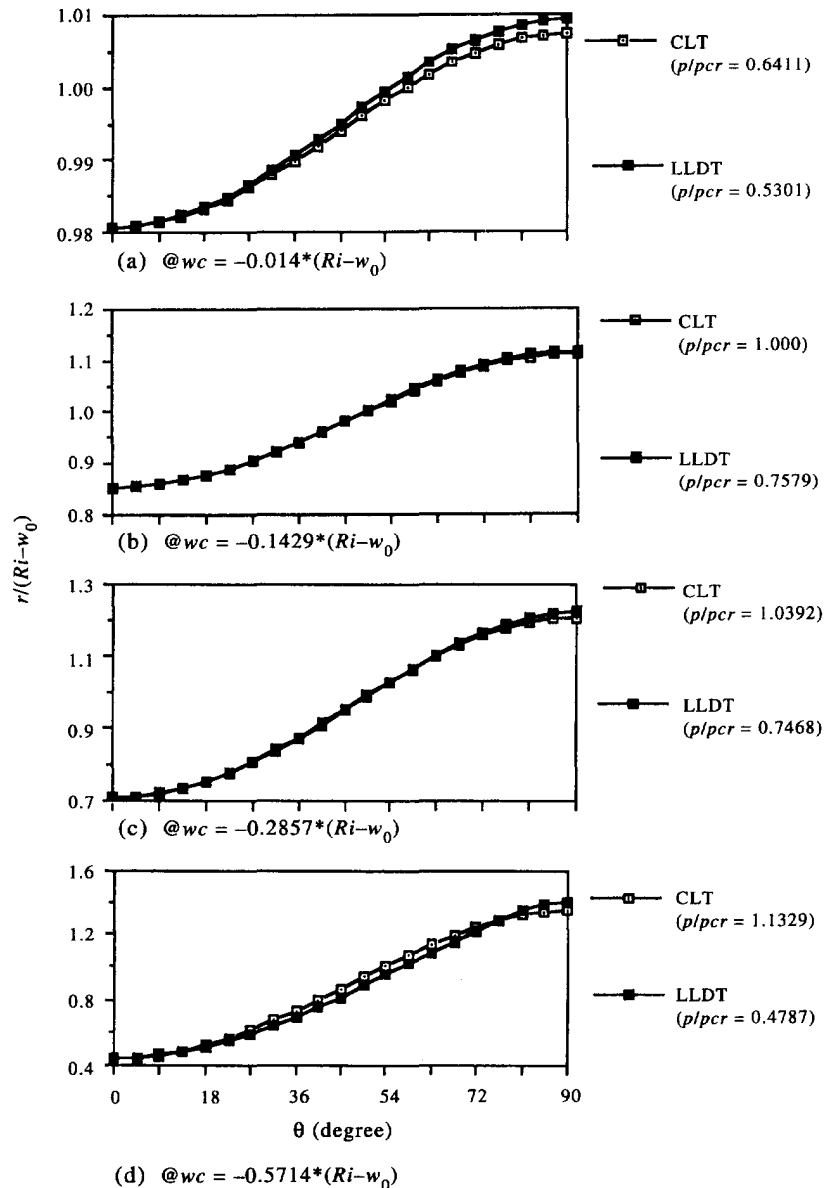
Fig. 10. Deformed shapes of the thick composite [90/0/90] cylinder computed using CLT and LSDT $(R_i/h = 6.0, w_0 = 0.005*R_i)$.

resembles the CLT solution for $R_i/h = 6$, shown in Fig. 8. As has been discussed in connection with Fig. 8, the appearance of a limit point on the elastic postbuckling equilibrium path is a measure of the degree of the effect of interlaminar shear/normal deformation. In contrast, a recent study on moderately thick ($R_i/h = 17.4$) isotropic rings has shown that their elastic postbuckling behavior is insensitive to modal imperfections, and the appearance of a limit point is solely due to the effect of inelastic constitutive relations (see Kim and Chaudhuri, to be published).

Variation of the normalized peak (collapse) pressure, p_{max}/p_{cr} with respect to the thickness parameter, R_i/h, is shown in Fig. 12. Magnitude of the normalized maximum (collapse) pressure, p_{max}/p_{cr}, is very sensitive to the thickness parameter, R_i/h. It is interesting to observe from Figs 11 and 12 that for thin [90/0/90] cylindrical shells the normalized maximum (collapse) pressure, p_{max}/p_{cr}, can be larger than unity by as much as 30–50% until for very thin cylinders, the elastic postbuckling path is completely stable as predicted by the classical laminating theory (CLT). For moderately thick cylinders, p_{max}/p_{cr} is close to
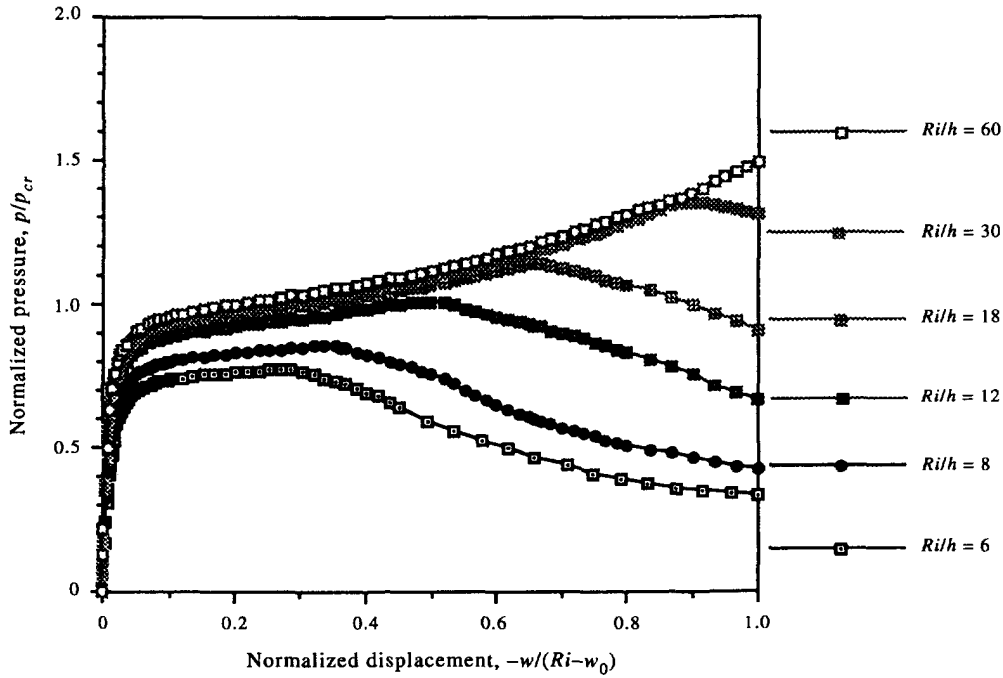
Fig. 11. Computed equilibrium paths of a composite [90/0/90] cylinder ($w_0 = 0.005*R_i$) for different radius to thickness ratios.
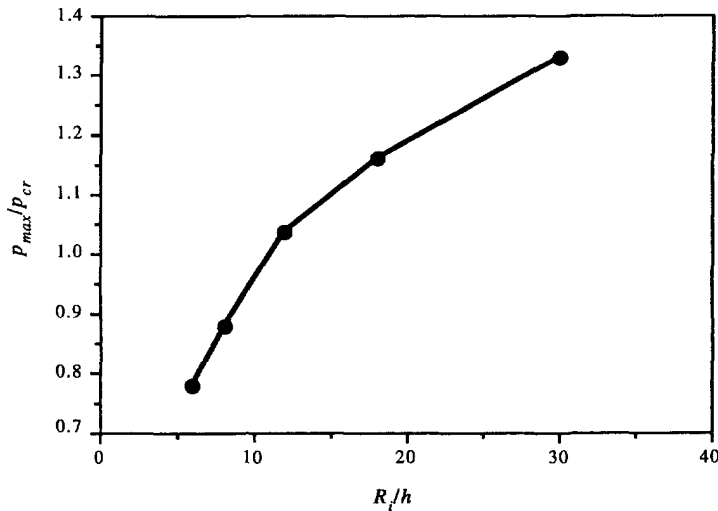
Fig. 12. Dependence of normalized maximum pressure on the radius to thickness ratio.

unity, while for thick cylinders, p_{max}/p_{cr} can be lower than unity by as much as 22% and beyond.

A qualitative understanding of the initiation of the shear crippling (kinkband) process and subsequent kinkband propagation along the axial length of a thick long cross-ply cylindrical shell can be obtained by considering the relation of applied pressure acting upon a circumferential arc length c_k, representing a fiber misalignment region, of a cylindrical section of unit axial length (force) to the deflection as shown in Fig. 13. The qualitative argument for initiation of shear crippling or kinkband in a thick cylindrical shell is similar to that for a number of localization phenomena—necking of metal bars in tension (G'sell et al., 1983; Hutchinson and Neale, 1983), initiation of bulging in a party balloon (Chater and Hutchinson, 1984), and various kinds of phase transition phenomena mentioned earlier. The shear crippling or kinkband is a phenomenon associated with localization of the postbuckling deformation pattern in a manner described by Tvergaard and Needleman
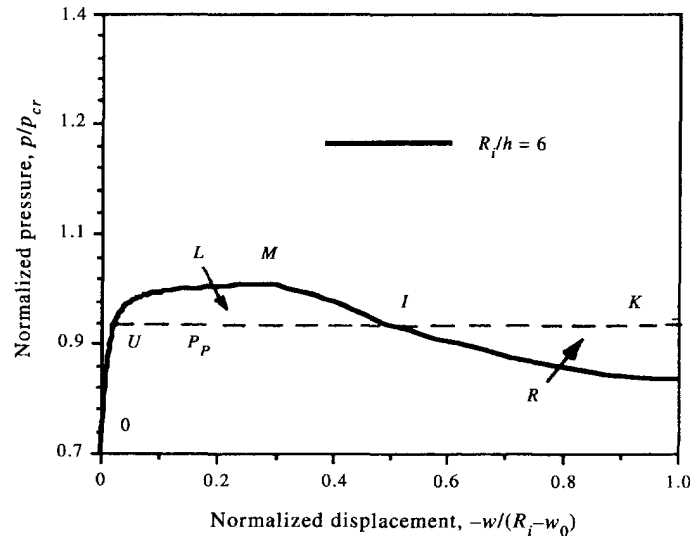
Fig. 13. Maxwell diagram for computation of propagation pressure in a thick cylinder ($R_i/h = 6.0$, $w_0 = 0.005*R_i$).

(1980). The details of the localization behavior in the context of interlaminar shear deformation at the lamina level are currently under investigation, and will be reported in a future paper. As has been pointed out by Chater and Hutchinson (1984), unlike tensile necking in common metals and many other problems involving localized instability modes, and like the bulges in party balloons and buckles in pipelines, the shear crippling starts to spread as the pressurization is continued. The present investigation is concerned with the steady state pressurization under a sufficiently slow rate of pumping of fluid (oil) into the pressure tank such that inertial effects are negligible (see Garala, 1989).

It may be noted here that Chater and Hutchinson (1984) in their study on the propagation of bulges and buckles considered the change in volume of a party balloon or the change in area of the plane strain ring in computing the work done by the applied pressure. This is because they were interested in computing the propagation bulge or buckle pressure involving more or less the entire cross-section of the plane strain ring. In contrast, the present investigation is primarily concerned with the propagation of kinkband arising out of a fiber misalignment region (assumed to be uniform through thickness), which occupies a very small portion of the circumference ($c_k \ll 2\pi R_m$). Since c_k is very small, $p(w)$ can be assumed to be constant over c_k. It is further noteworthy from Fig. 13 that for the same pressure a point within the segment of length c_k can occupy any of the three deflected positions, e.g. U, I and K, and that the hump UMI acts as a potential barrier in analogy to a two-well potential problem. It takes some energy to cross the barrier, which is provided in this case by the elastic strain energy released by the kinking fibers triggered by fiber misalignment defects. Similar pressure–deflection plots can be obtained for points located within a finitely large number of segments outside of the fiber misalignment region. However, since there is no supply of energy to cross the barrier, these points are likely to occupy deflected positions in the OUM branch. This qualitatively explains the localization of the deformation pattern within the plane strain ring subjected to hydrostatic pressure, which is entirely different from the modal ($n = 2$) deformation pattern represented by the CLT solution in Fig. 8. Furthermore, this localization of deformation within a very narrow band is different from that of plastic buckle resulting in flattening of a long pipeline, studied by Chater and Hutchinson (1984), and Kyriakides (1994). Spreading or propagation of the shear crippling or kinkband instability is generally associated with the upturn in the curve of pressure acting upon the circumferential arc length c_k, representing a fiber misalignment region, of a cylindrical section of unit axial length (force) vs deflection (Fig. 13). The increasing resistance after the hypothesized touching of a kinked section to further deflection terminates the localization process, and forces the kink band to propagate longitudinally into the neighboring section. Before this happens, the pressurization process reaches a

steady state in which the pressure is constant. It may be noted here that since the failure (shear) strain of a carbon fiber reinforced cross-ply thick cylinder under consideration is very limited unlike that of latex rubber balloon or a moderately thick metallic pipeline material, the maximum deflection in the present study will not be large enough for actual touching of two diametrically opposite points to materialize. However, as Kyriakides (1994) has pointed out, the up-down-up feature of the pressure–deflection plot is essential for a propagating instability. Therefore, in the case of the plane strain carbon composite cross-ply ring, the hypothetical touching, and subsequent rigid or elastic rebound is a computational formalism, noting that the propagating kinkband pressure, which corresponds to the failure strain of carbon fibers is well above the pressure plateau of Fig. 13.

The criterion for determining the quasi-static propagation pressure, p_P, under steady state conditions, can be derived from the energy balance requirement that the work done by the applied pressure acting upon the circumferential arc length c_k, representing a fiber misalignment region, of a cylindrical section of a unit axial length must equal the change of strain energy stored in the same portion of the cylindrical arc segment in any advance of the kinkband in the axial direction of the cylinder. This is illustrated for a thick [90/0/90] cylinder ($R_i/h = 6$) in Fig. 13. The transition front between the shear-crippled or kinked cylindrical segment, and its unkinked counterpart is considered to be fixed which simply translates in the axial direction of the cylinder. The work done by the pressure acting upon the circumferential arc length c_k, representing a fiber misalignment region, of a cylindrical section of unit axial length, p_P, in shifting the transition front in the axial direction of the cylinder is given by $c_k p_P(w_U - w_K)$, where the subscripts, U and K denote unkinked and kinked segments, respectively (see Fig. 13). This external work of the pressure is equal to the internal work, ΔW, done on a circumferential arc length c_k, representing a fiber misalignment region of a cylinder section of unit axial length as it passes from the state U to the state K through the transition. Since the deformation is purely elastic, a strain energy function is path-independent, which suggests that ΔW is independent of the details of the deformation history in the transition and depends only on the end states, U and K. The strain energy stored is then given by $\Delta W = c_k \int_U^K p(w)\,dw$. Finally, equating the external work to the internal work yields the equation for the external pressure, for quasi-static steady state kinkband propagation

$$c_k p_P(w_U - w_K) = c_k \int_U^K p(w)\,dw. \tag{58}$$

Equation (58) has a simple graphical solution which is known in the literature of phase transition as the Maxwell construction involving conjugate thermodynamical variables for two co-existing phases (Pathria, 1977). The physical basis of the Maxwell construction is given by the principle of minimum Helmholtz free energy. In regards to the problem under consideration, equality of the rectangular area $c_k p_P(w_U - w_K)$ and the area under the pressure–deflection curve $c_k \int_U^K p(w)\,dw$ is equivalent to the condition that the two area lobes, L and R in Fig. 13, be equal.

In analogy to what is well-known in the phase transition literature, the slope of p vs $w^* = -w/(R_i - w_0)$ curves (Figs 8, 11, 13), can never be negative. These curves represent iso-thickness-shear states, which are analogous to isotherms of the phase transition literature. While in the absence of any localized fiber waviness or misalignments, the slope may be expected to be positive until failure, the presence of such defects, representing initial thickness shear strains, can cause a region with zero slope to exist, whereby the structure may nearly lose its stiffness. The existence of such a region in the p vs w^* diagram corresponds to the coexistence of two "phases", i.e. a highly localized band of kinked or shear crippled "phase", and its unkinked counterpart in the rest of the cylinder. In analogy to the phase transition phenomena, the fiber misalignments may be treated as impurities or dopants. An understanding analogous to how impurities localize electron states in condensed matter (see Zee, 1995) is essential for understanding the experimentally observed
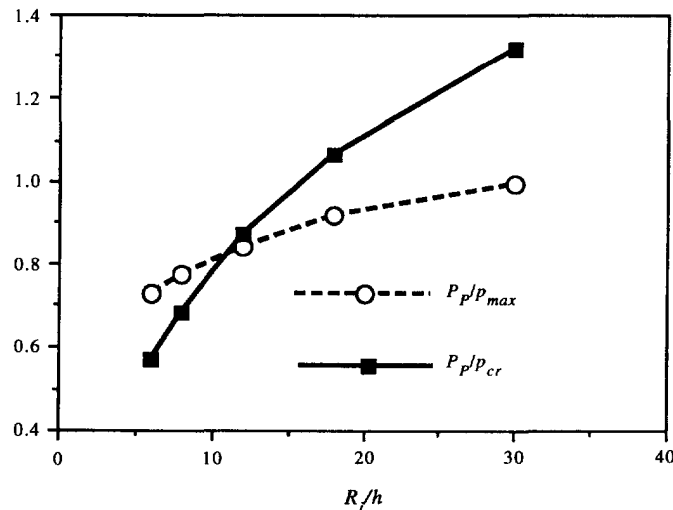
Fig. 14. Dependence of normalized propagation pressure on the radius to thickness ratio.

(see Chaudhuri, 1991; Garala, 1989; Garala and Chaudhuri, 1993) localization of quasi-statically propagating kink bands being initiated at the fiber misalignment sites. The aforementioned zero slope constitutes a direct evidence of the onset of "phase" transition in the system. It is worthwhile to note in this connection that as long as one uses the exact micro-structural geometry and exact micro-mechanically derived constitutive relations for modeling the initial fiber waviness, the unphysical region of negative slope in the p vs w^* diagram would never appear. The appearance of such an unphysical region in the present case is then a direct consequence of assumption of uniform fiber alignment in a lamina, because it is nearly impossible to introduce the micro-structural geometry, such as waviness in 6–10 micron diameter carbon fibers and 0.5–1 micron thick interphase, in a macro-structural modeling tool such as the finite elements methods. This assumption eliminates the very possibility of the structural system passing through a state or region of flatness in the p vs w^* diagram, in which there coexist two "phases" of different transverse shear strains. This discrepancy is corrected by the Maxwell construction of equal areas in Fig. 13. The Maxwell construction then implies the possibility that under favorable conditions, such as the presence of severe localized fiber misalignment defects, the equilibrium configuration of the externally pressurized composite cylinder will involve a multi-"phase"— i.e. localized (quasi-statically propagating) kinkband and its unkinked counterpart—state. It is further noteworthy that the observed microstructural ordering of the shear-kinked fibers in a localized kink band (see Chaudhuri, 1991) is analogous to long range order that arises in the case of collective states of condensed media formed under phase transition of the second kind, such as superfluidity of liquid helium, and the superconductivity and ferromagnetism of metals, which exist only at temperatures below the critical temperature (see Popov and Yarunin, 1988).

Figure 14 shows the variation of the propagation pressure, p_P, normalized by classical buckling pressure of the perfect cylinder, p_{cr}, with respect to the radius to thickness ratio, R_i/h. Sensitivity of the normalized propagation pressure to the radius-to-thickness ratio is self-evident in this plot. For example, as has been mentioned above, for a very thin cylindrical shell ($R_i/h \geqslant 40$ approx.), the pressure–deflection plot does not exhibit a limit point. The elastic postbuckling path is, in this case, stable, and the question of localization or limit point behavior does not arise. This type of structure is not expected to experience a catastrophic localized failure mode in the absence of inelasticity. For relatively thin cylinders, $16 < R_i/h \leqslant 30$–40 (approx.), a limit point appears on the postbuckling equilibrium path followed by negative slope, which might, at first sight, seem surprising from a purely macroscopic point of view, because: (a) the elastic postbuckling behavior of a long cylinder (plane strain) or a ring (plane stress) is stable in the absence of interlaminar shear deformation and (b) only an inelastic postbuckling path of a ring is known to exhibit a

limit point and negative slope beyond this point. However, in view of the micro-structural interaction studied in this paper at the lamina level and its analogy to the phase transition phenomena discussed above, this kind of postbuckling behavior (i.e. appearance of a limit point and negative slope beyond, which is associated with the spontaneous symmetry breaking) can justifiably be expected. Nonetheless, since the propagation pressure p_P is greater than p_{cr}, the global or structural stable postbuckling precedes, in the absence of inelasticity, a catastrophic localized failure mode, thus providing some margin of safety for this type of structure. For moderately thick cylindrical shells ($R_i/h \leqslant 16$ approx.), the normalized propagation pressure p_P/p_{cr} is less than unity, implying the dominance of the catastrophic localized shear crippling or kinkband type failure mode (even in the absence of inelasticity), which leaves little margin of safety. However, in view of the micro-structural interaction studied in this paper at the lamina level and its analogy to the phase transition phenomena discussed above, this kind of postbuckling behavior (i.e. p_P/p_{cr} is less than unity) is to be expected below a critical R_i/h ratio, which is analogous to the critical temperature for superfluidity of liquid helium and superconductivity of metals. The $R_i/h \sim 16$ (approx.) then serves as the critical (bottom surface) radius-to-thickness ratio for the composite cylinder under investigation. For very thick cylindrical shells, e.g. $R_i/h \leqslant 6$, the normalized propagation pressure p_P/p_{cr} is of the order of 0.57 or less, which qualitatively explains the sudden and violently catastrophic failure of these cylinders under hydrostatic pressure due to kinkband propagation along the entire length of such cylinders, observed by Garala and coworkers. Figure 14 also shows the propagating pressure normalized with respect to peak (collapse) pressure, p_P/p_{max}, is close to unity for a relatively thin cylinder ($R_i/h = 30$), and drops with the increase of thickness to a value as low as 0.726 for a very thick cylinder ($R_i/h = 6$).

7. SUMMARY AND CONCLUSIONS

A fully nonlinear analysis for prediction of shear crippling (kinkband) type propagating instability in long thick laminated composite cylindrical shells is presented. The primary accomplishment of the present investigation is prediction of equilibrium paths, which are often unstable, in the presence of interlaminar shear deformation, and which usually deviate from the classical lamination theory (CLT)-based equilibrium paths, representing global or structural level instability. A nonlinear finite element methodology, based on a three-dimensional hypothesis, known as layerwise linear displacement distribution theory (LLDT) and the total Lagrangian formulation, is developed to predict the aforementioned instability behavior of long laminated thick cylindrical shell type structures and evaluate failure modes when radial/hydrostatic compressive loads are applied. The most important computational features is the successful implementation of an incremental displacement control scheme beyond the limit point to compute the unstable postbuckling path, without completely changing the system matrix (i.e. partitioning or destroying the original skyline of the total stiffness matrix that is used to compute the prebuckling solution). A long (plane strain) thick laminated composite [90/0/90] imperfect cylinder is investigated with the objective of analytically studying its premature compressive failure behavior. Thickness effect (i.e. interlaminar shear/normal deformation) is clearly responsible for causing the appearance of limit point on the postbuckling equilibrium path, thus lowering the load carrying capability of the long composite cylinder, and localizing the failure pattern. Finally, interlaminar shear crippling or kinkband type propagating instability triggered by the combined effect of interlaminar shear/normal deformation and geometric imperfections, such as fiber misalignment, appears to be one of the dominant compressive failure modes. What follows is a list of useful conclusions drawn from the numerical results of the present investigation:

(i) Numerical results on symmetrically laminated [90/0/90] moderately thick and thick long cylindrical shells (plane strain) with modal imperfections show that a stable postbuckling solution is obtained when the classical lamination theory (CLT) is used. However, in contrast to the CLT solution, a limit point appears on the postbuckling path computed

using the LLDT, even in the linear elastic material case, which results in significant reduction of the maximum (collapse) pressure (e.g. 21.7% of the CLT based linearized buckling pressure in the case of $R_i/h = 6.0$). The interlaminar shear/normal deformation causes the appearance of this distinct limit point that represents the collapse pressure, beyond which the equilibrium path is unstable, and as a result, an elastic shear deformable plane strain laminated composite ring is imperfection sensitive.

(ii) It may be noted that because the structure cannot follow an unstable equilibrium path, it will switch to a localization mode with a significant drop of the load carrying capacity of the composite [90/0/90] plane strain ring under investigation. In analogy to phase transition phenomena in condensed matter physics, this represents a long range order (of nonlocal or gage theories) that is intimately connected with spontaneous symmetry breaking. In the example problem studied, localization of the deformation pattern is associated with spontaneous breaking of the periodicity of classical or modal buckling patterns.

(iii) As the value of shear modulus, G_{LT} decreases, the LLDT-based solution deviates further from its CLT based counterpart. It is further concluded that the classical lamination theory (CLT) is not suitable for obtaining an accurate load–displacement solution of a composite cylinder with low shear modulus to longitudinal Young's modulus ratio, which characterizes the carbon fiber reinforced composites.

(iv) The limit point is delayed as the radius to thickness ratio increases (i.e. as the effect of interlaminar shear/normal deformation decreases), and finally disappears in the very thin cylinder case ($R_i/h = 60$ and beyond), which is to be expected in accordance with the CLT. The latter resembles the CLT solution for $R_i/h = 6$.

(v) Variation of the normalized peak (collapse) pressure, p_{max}/p_{cr} with respect to the thickness parameter, R_i/h, shows that the magnitude of the normalized maximum (collapse) pressure, p_{max}/p_{cr}, is very sensitive to the thickness parameter, R_i/h. It is interesting to observe that for thin [90/0/90] cylindrical shells the normalized maximum (collapse) pressure, p_{max}/p_{cr}, can be larger than unity by as much as 30–50% until for very thin cylinders, the elastic postbuckling path is completely stable as predicted by the classical lamination theory (CLT). For moderately thick cylinders, p_{max}/p_{cr}, is close to unity, while for thick cylinders, p_{max}/p_{cr}, can be lower than unity by as much as 22% and beyond.

(vi) The Maxwell construction implies the possibility that under favorable conditions, such as the presence of severe localized fiber misalignment defects, the equilibrium configuration of the externally pressurized composite cylinder will involve a multi-"phase"— i.e. localized (quasi-statically propagating) kinkband and its unkinked counterpart—state. It is further noteworthy that the observed microstructural ordering of the shear-kinked fibers in a localized kinkband (see Chaudhuri, 1991) is analogous to long range order that arises in the case of collective states of condensed media formed under phase transition of the second kind, such as superfluidity of liquid helium, and the superconductivity and ferromagnetism of metals, which exist only at temperatures below the critical temperature.

(vii) Sensitivity of the normalized propagation pressure to the radius-to-thickness ratio, R_i/h is self-evident in this investigation. For example, for a very thin long cylindrical shell ($R_i/h \geq 40$ approx.), the pressure–deflection plot does not exhibit a limit point. The elastic postbuckling path is, in this case, stable, and the question of limit point or localization behavior does not arise. This type of structure is not expected to experience a catastrophic localized failure mode in the absence of inelasticity.

(viii) For relatively thin cylinders, $16 < R_i/h \leq 30$–40 (approx.), a limit point appears on the postbuckling equilibrium path followed by negative slope, which might, at first sight, seem surprising from a purely macroscopic point of view, because: (a) the elastic postbuckling behavior of a long cylinder (plane strain) or a ring (plane stress) is stable in the absence of interlaminar shear deformation and (b) only an inelastic postbuckling path of a ring is known to exhibit a limit point and negative slope beyond this point. However, in view of the micro-structural interaction studied in this paper at the lamina level and its analogy to the phase transition phenomena discussed above, this kind of postbuckling behavior (i.e. appearance of a limit point and negative slope beyond, which is associated with the spontaneous symmetry breaking) can justifiably be expected. Nonetheless, since the propagation pressure p_P is greater than p_{cr}, the global or structural stable postbuckling

precedes, in the absence of inelasticity, a catastrophic localized failure mode, thus providing some margin of safety for this type of structure.

(ix) For moderately thick cylindrical shells ($R_i/h \leqslant 16$ approx.), the normalized propagation pressure p_P/p_{cr} is less than unity, implying the dominance of the catastrophic localized shear crippling or kinkband type failure mode (even in the absence of inelasticity), which leaves little margin of safety. However, in view of the micro-structural interaction studied in this paper at the lamina level and its analogy to the phase transition phenomena discussed above, this kind of postbuckling behavior (i.e. p_P/p_{cr} is less than unity) is to be expected below a critical R_i/h ratio, which is analogous to the critical temperature for superfluidity of liquid helium and superconductivity of metals. The $R_i/h \sim 16$ (approx.) then serves as the critical (bottom surface) radius-to-thickness ratio for the long composite cylinder under investigation.

(x) For very thick cylindrical shells, e.g. $R_i/h \leqslant 6$, the normalized propagation pressure p_P/p_{cr} is of the order of 0.57 or less, which qualitatively explains the sudden and violently catastrophic failure of these cylinders under hydrostatic pressure due to experimentally observed kinkband propagation along the entire length of such cylinders.

(xi) The propagation pressure normalized with respect to peak (collapse) pressure, p_P/p_{max}, is close to unity for a relatively thin cylinder ($R_i/h = 30$), and drops with the increase of thickness to a value as low as 0.726 for a very thick cylinder ($R_i/h = 6$).

(xii) Onset of the interlaminar shear crippling or kinkband type propagating instability triggered by the combined effect of interlaminar shear/normal deformation and imperfection at the microstructural (i.e. lamina) level appears to be the dominant compressive failure mode. Structural buckling or limit load can be attained, only if the lamina material can survive this microstructure related instability failure.

(xiii) A three-dimensional theory, such as LLDT, is essential for capturing the interlaminar shear crippling propagating instability triggered by the combined effect of interlaminar shear/normal deformation and geometric imperfections.

The present investigation reveals that the formation and propagation of localized shear crippling patterns triggered by the interlaminar shear/normal deformation may lead to a premature catastrophic failure of the imperfect cross-ply long cylinders investigated here unless ultimate shear strain of the lamina material is sufficiently high. In other words, it will be possible to enhance the compressive strength by using composite materials of somewhat higher shear moduli and substantially higher ultimate shear strains. The possibility of the compressive strength being enhanced up to the point of macrostructural collapse, p_{max}, exists, if the lamina material survives the microscopically observed fiber kinking failure leading to the shear crippling failure at the macroscopic level. One possible remedy is the use of commingled (at the tow level) hybridized carbon/glass fibers reinforced composite materials that have shown some promise for arresting the microstructural level kinking failure (see Chaudhuri and Garala, 1995). These measures are expected to result in the design of more defect tolerant composite cylinders for deep submergence applications.

REFERENCES

Abdallah, M. G., Gascoigne, H. E., Cairnes, D. S. and Patton, K. B. (1990). Measurement of deformation in thick composite rings subjected to external pressure. Presented at SEM's Spring Conference on Experimental Mechanics and Manufacturer's Exhibit, Albuquerque, N.M.

Batoz, J. L., Chattopadhyay, A. and Dhatt, G. S. (1976). Finite element large deflection analysis of shallow shells. *International Journal of Numerical Methods in Engineering* 10, 39–58.

Batoz, J. L. and Dhatt, G. (1979). Incremental displacement algorithms for nonlinear problems. *International Journal of Numerical Methods in Engineering* 15, 1262–1267.

Bert, C. W. (1986). Falling dominoes. *SIAM Review* 28, 219–224.

Chater, E. and Hutchinson, J. W. (1984). On the propagation of bulges and buckles. *ASME Journal of Applied Mechanics* 51, 269–277.

Chaudhuri, R. A. (1991). Prediction of the compressive strength of thick-section advanced composite laminates. *Journal of Composite Materials* 25, 1244–1276.

Chaudhuri, R. A. and Garala, H. J. (1995). Analytical/experimental evaluation of kink toughness in hybrid commingled carbon/glass/epoxy thick-section composites under compression. *Journal of Composite Materials* **29**, 1695–1718 (see also the Errata).

Chaudhuri, R. A., Kim, D. J. and Hsia, R. L. (to be published). Effect of thickness and lamination on the large deflection behavior of laminated shells.

Garala, H. J. (1986). Structural evaluation of externally pressurized, 4-inch diameter, graphite-composite cylinder. DTRC (NSWC) Report 86-071.

Garala, H. J. (1989). Structural evaluation of 8-inch diameter graphite–epoxy composite cylinders subjected to external hydrostatic compressive loading. DTRC (NSWC) Report 89/016.

Garala, H. J. and Chaudhuri, R. A. (1993). Structural evaluation of advanced composite thick-section cylinders under biaxial compression. In *Mechanics of Thick Composites* (Edited by Y. Rajapakse), AMD-Vol. 162, pp. 227–236.

Green, A. E. and Zerna, W. (1968). *Theoretical Elasticity*. Clarendon Press, Oxford.

G'Sell, C., Aly-Helal, N. A. and Jonas, J. J. (1983). Effect of stress triaxiality of neck propagation during the tensile stretching of solid polymers. *Journal of Materials Science* **18**, 1731–1742.

Hsia, R. L. and Chaudhuri, R. A. (in press). Geometrically nonlinear analysis of cylindrical shells using surface-parallel quadratic elements. *Computers & Structures*

Hutchinson, J. W. and Neale, K. W. (1983). Neck propagation. *Journal of Mechanics and Physics of Solids* **31**, 405–426.

Jones, R. M. and Morgan, H. S. (1975). Buckling and vibration of cross-ply laminated circular cylindrical shells. *AIAA Journal* **13**, 664–671.

Kim, D. J. and Chaudhuri, R. A. (1995). Full and von Karman geometrically nonlinear analyses of laminated cylindrical panels. *AIAA Journal* **33**, 2173–2181.

Kim, D. J. and Chaudhuri, R. A. (to be published). Nonlinear analysis of moderately thick rings with modal imperfections.

Koiter, W. T. (1945). The stability of elastic equilibrium (in Dutch) (Edited by H. J. Paris). Ph.D. Thesis, Delft, The Netherlands.

Korn, G. A. and Korn, T. M. (1968). Differential geometry. In *Mathematical Handbook*, Ch. 17, Second Edition, McGraw-Hill, New York.

Kyriakides, S. (1994). Propagation instabilities in structures. In *Advances in Applied Mechanics* (Edited by J. W. Hutchinson and T. Y. Wu), Vol. 30, Academic Press, Boston.

Noor, A. K. and Burton, W. S. (1990). Assessment of computational models for multilayered composite shells. *Applied Mechanics Review* **43**, 67–97.

Pathria, R. K. (1977). *Statistical Mechanics*. Pergamon, Oxford.

Popov, V. N. and Yarunin, V. S. (1988). *Collective States in Quantum Statistics of Radiation and Matter*. Kluwer Academic, Dordrecht, The Netherlands.

Seide, P. and Chaudhuri, R. A. (1987). Triangular finite element for analysis of thick laminated shells. *International Journal of Numerical Methods in Engineering* **24**, 1563–1579.

Simitses, G. J. (1986). Buckling and postbuckling of imperfect cylindrical shells: a review. *Applied Mechanics Review* **39**, 1517–1524.

Starnes, J. and Williams, J. G. (1982). Failure characteristics of gr/epoxy structural components loaded in compression. NASA TM 84552.

Waas, A. M., Babcock, C. D. and Knauss, W. G. (1990). An experimental study of compression failure of fibrous laminated composites in the presence of stress gradients. *International Journal of Solids and Structures* **26**, 1071–1098.

Thomas, G. and Gallagher, R. H. (1975). A triangular thin shell finite element: nonlinear analysis. NASA CR-2483, Washington, D.C.

Tvergaard, V. and Needleman, A. (1980). On the localization of buckling patterns. *ASME Journal of Applied Mechanics* **47**, 613–619.

Zee, A. (1995). Quantum hall fluids. In *Field Theory, Topology and Condensed Matter Physics* (Edited by H. B. Geyer), pp. 99–153. Springer, Berlin.

Zienkiewicz, O. C. (1971). Incremental displacement in nonlinear analysis. *International Journal of Numerical Methods in Engineering* **3**, 587–592.

APPENDIX

The matrix $[B_{LL}]$ referred to in eqn (26a) is given as shown below:

$$[B_{LL}] = \begin{bmatrix} \dfrac{\partial}{\partial x^1} & 0 & 0 \\[2mm] 0 & \dfrac{1}{g_\beta}\dfrac{\partial}{\partial x^2} & \dfrac{1}{g_\beta} \\[2mm] 0 & 0 & \dfrac{\partial}{\partial z} \\[2mm] 0 & \dfrac{\partial}{\partial z} & \dfrac{1}{g_\beta}\dfrac{\partial}{\partial x^2} \\[2mm] \dfrac{\partial}{\partial z}-\dfrac{1}{g_\beta} & 0 & \dfrac{\partial}{\partial x^1} \\[2mm] \dfrac{1}{g_\beta}\dfrac{\partial}{\partial x^2} & \dfrac{\partial}{\partial x^1} & 0 \end{bmatrix}. \tag{A1}$$

The matrix $[B_{\text{NL}}]$ referred to in eqn (26b) is given as follows:

$$[B_{\text{NL}}] = [[B_{\text{NL1}}] \quad [B_{\text{NL2}}] \quad [B_{\text{NL1}}]] \tag{A2}$$

where

$$[B_{\text{NL1}}] = \begin{bmatrix} R_{11} \dfrac{\partial}{\partial x^1} \\[2ex] \dfrac{R_{21}}{g_\beta} \dfrac{\partial}{\partial x^2} \\[2ex] R_{31} \dfrac{\partial}{\partial z} \\[2ex] \dfrac{R_{31}}{g_\beta} \dfrac{\partial}{\partial x^2} + R_{21} \dfrac{\partial}{\partial z} \\[2ex] R_{31} \dfrac{\partial}{\partial x^1} + R_{11} \dfrac{\partial}{\partial z} \\[2ex] \dfrac{R_{11}}{g_\beta} \dfrac{\partial}{\partial x^2} + R_{21} \dfrac{\partial}{\partial x^1} \end{bmatrix} \tag{A3a}$$

$$[B_{\text{NL2}}] = \begin{bmatrix} R_{12} \dfrac{\partial}{\partial x^1} \\[2ex] \dfrac{R_{22}}{g_\beta} \dfrac{\partial}{\partial x^2} - \dfrac{R_{23}}{g_\beta} \\[2ex] R_{32} \dfrac{\partial}{\partial z} \\[2ex] R_{22} \dfrac{\partial}{\partial z} + \dfrac{R_{32}}{g_\beta} \dfrac{\partial}{\partial x^2} - \dfrac{R_{33}}{g_\beta} \\[2ex] R_{32} \dfrac{\partial}{\partial x^1} + R_{12} \dfrac{\partial}{\partial z} \\[2ex] R_{22} \dfrac{\partial}{\partial x^1} + R_{12} \dfrac{\partial}{\partial x^2} - \dfrac{R_{13}}{g_\beta} \end{bmatrix} \tag{A3b}$$

$$[B_{\text{NL3}}] = \begin{bmatrix} R_{13} \dfrac{\partial}{\partial x^1} \\[2ex] \dfrac{R_{23}}{g_\beta} \dfrac{\partial}{\partial x^2} + \dfrac{R_{22}}{g_\beta} \\[2ex] R_{33} \dfrac{\partial}{\partial z} \\[2ex] \dfrac{R_{32}}{g_\beta} \dfrac{g_2}{\rho} + \dfrac{R_{33}}{g_\beta} \dfrac{\partial}{\partial x^2} + R_{23} \dfrac{\partial}{\partial z} \\[2ex] R_{33} \dfrac{\partial}{\partial x^1} + R_{13} \dfrac{\partial}{\partial z} \\[2ex] R_{23} \dfrac{\partial}{\partial x^1} + \dfrac{R_{13}}{g_\beta} \dfrac{\partial}{\partial x^2} + \dfrac{R_{12}}{g_\beta} \end{bmatrix} \tag{A3c}$$

in which

$$\{R_{ij}\} = [B_{\text{NN}}]\{\bar{\mathbf{v}}\} \tag{A4}$$

with

$$\{R_{ij}\} = \{R_{11} \quad R_{12} \quad R_{13} \quad R_{21} \quad R_{22} \quad R_{23} \quad R_{31} \quad R_{32} \quad R_{33}\}^T \tag{A5}$$

$$\{\bar{\mathbf{v}}\} = \{\bar{u} \quad \bar{v} \quad \bar{w}\}^T \tag{A6}$$

R. A. Chaudhuri and D. Kim

where the components of the vector $\bar{\mathbf{v}}\}$ are known displacements at time t. The matrix $[B_{NN}]$ referred to in eqns (26c) and (A4) is given as follows:

$$[B_{NN}] = \begin{bmatrix} \dfrac{\partial}{\partial x^1} & 0 & 0 & \dfrac{1}{g_\beta}\dfrac{\partial}{\partial x^2} & 0 & 0 & \dfrac{\partial}{\partial z} & 0 & 0 \\[2ex] 0 & \dfrac{\partial}{\partial x^1} & 0 & 0 & \dfrac{1}{g_\beta}\dfrac{\partial}{\partial x^2} & -\dfrac{1}{g_\beta}\dfrac{g_2}{\rho} & 0 & \dfrac{\partial}{\partial z} & 0 \\[2ex] 0 & 0 & \dfrac{\partial}{\partial x^1} & 0 & \dfrac{1}{g_\beta}\dfrac{g_2}{\rho} & \dfrac{1}{g_\beta}\dfrac{\partial}{\partial x^2} & 0 & 0 & \dfrac{\partial}{\partial z} \end{bmatrix}^{\mathrm{T}} . \tag{A7}$$